POLITECNICO DI TORINO

Master's Degree in Aerospace Engineering

Master's Thesis

Investigation of beamforming techniques for rotating noise sources

Supervisors

Prof. Christophe SCHRAM

Prof. Renzo ARINA

Dr. Riccardo ZAMPONI

Dr. Alessandro ZARRI

Candidate

Valerio SCOLLO

April 2022

Abstract

Over the last few decades, acoustic beamforming methods with phased microphone arrays have gained increasing attention from both industries and research institutes, providing a practical tool for acoustic-field investigations in wind-tunnel tests and achieving accurate results. The purpose of this Master Thesis is to provide a detailed overview of the main beamforming algorithms for the localization and quantification of sound sources generated by rotating machines, such as wind turbines, low-pressure fans, and low-speed propellers, as well as a thorough understanding of their potential and inner limits.

The time-domain ROtating Source Identifier (ROSI) method and the frequency-domain Virtual Rotating Array Method (VRAM) method are currently the most widely used beamforming techniques in the acoustic community. The first one provides satisfactory results regardless of the geometry and spatial position of the microphone array, but it requires significant processing time and does not allow for the application of advanced beamforming methods. The second one supports advanced beamforming methods and decreases the computational cost considerably but is constrained by the microphone array shape and its position in relation to the inspected item. A mesh-based VRAM extension for irregularly shaped microphone arrays is developed and optimized to merge the benefits of both techniques. Its overall performance has been evaluated using two different synthetic benchmarks that feature monopolar rotating sources emitting white noise, yielding blurred beamforming maps with lower sound power levels and discouraging further investment in this direction.

Furthermore, the CleanT deconvolution approach has been implemented and tested to meet the necessity of overcoming conventional beamforming limits, achieving good performances in finding the exact position of sound sources in rotating frames.

Finally, all these methods have been employed to characterize the sound sources in an un-skewed low-pressure axial fan, highlighting the prevalence of leading-edge noise at lower frequencies and self-noise at higher frequencies. This latter investigation demonstrates how effective these tools are in real-world applications, resulting in a better understanding of the noise generation mechanisms underlying rotating devices.

Table of Contents

List of Tables

List of Figures

Nomenclature

Acronyms

BW	Beamwidth
CB	Conventional Beamforming
CSM	Cross-spectral matrix
dB	deciBel
GIBF	Generalized Inverse BeamForming
N-S	Navier-Stokes
PSF	Point Spread Function
ROSI	ROtating Source Identifier
SLR	Sidelobe Ratio
SPL	Sound Pressure Level
VRAM	Virtual Rotating Array Method

Latin letters

c_0	Speed of sound
c_v	Specific heat at constant volume
d	Distance between microphones in an array
E	Total energy
f	Frequency
f_b	Body forces

f_c	Center frequency of a third-octave band
g_j	Steering vector related to the j-th scan grid point
i	$\sqrt{-1}$
I	Identity matrix
L_p	Sound pressure level
N	Microphones number
M	Mach number
p	Pressure
$q(\mathbf{y}, \tau)$	Acoustic source located in $\mathbf{y}$ and emitted at time: $t = \tau$
Q_m	Acoustic source due to a mass variation
Q_W	Acoustic source due to a heat variation
r	Radius
s	Entropy
s_j	Source intensity at the j-th scan grid point
t	Time
t_d	Time delay
T	Temperature
u	velocity among the x-direction
w_j	Weighted steering vector related to the j-th scan grid point

Greek letters

α	Angular distance between two adjacent microphones
γ	Specific heat ratio
$\Gamma^{(i)}$	Dirty map at the $i - th$ iteration
$\varepsilon_n(t_k)$	Noise perturbation perceived by the $n - th$ microphone at the sampling time k
$\zeta(\tau)$	Focus point location at the emitting time τ
θ	Angle between the source direction and the source-receiver one
λ	Acoustic signal wavelenght
μ	Viscosity coefficient

ρ	Density
τ	Emission time
$\varphi(t)$	Virtual rotating array angular position in function of time
$\Phi^{(i)}$	Clean map at the $i-th$ iteration
ω	Rotational speed

Symbols & Indices

$(\cdot)'$	Perturbation
$(\cdot)^T$	Transpose
$(\cdot)_0$	Constant value
$(\cdot)_{rms}$	Root mean square
$(\cdot)^{res}$	Residual value
$(\cdot)_{ref}$	Reference value
$(\cdot)^*$	Complex conjugate transpose
$\langle . \rangle$	Time average over several snapshots

Chapter 1

Introduction

1.1 The von Karman Institute for Fluid Dynamics

The von Karman Institute is a non-profit international educational and scientific organization that is at the forefront of fluid dynamics research. It was founded in 1956 and is named after its founder, Theodore von Karman; today, it houses three departments: Aeronautics & Aerospace, Environmental & Applied Fluid Dynamics and Turbomachinery & Propulsion. Extensive research on experimental, computational, and theoretical aspects of gas and liquid flows is conducted at the VKI under the supervision of faculty professors and research engineers and is primarily funded by governmental and international agencies, as well as industries. Furthermore, it provides post-graduate education programs such as the research master in fluid dynamics, doctoral programs, stagier programs, and lecture series, with the goal of encouraging "research training through research".

1.2 Problem explanation

According to the World Health Organization, noise pollution can cause seven types of negative health effects, including hearing impairment, interference with spoken communication, sleep disturbances, cardiovascular disturbances, disturbance in mental health, impaired task performance, and negative social behaviour [1]. To overcome this problem, regulatory bodies have worked hard over the last two decades, issuing acoustic emission standards. As a result, the interest in understanding sound generation mechanisms and the associated noise emissions has drawn the attention of the majority of aerospace companies

and research institutes, which have intensified both numerical and experimental campaigns in order to provide qualitative and quantitative results.
One of the most widespread experimental techniques, and the topic of this project, is acoustic beamforming whose purpose consists of spatial filtering an acquired signal by means of a phased array, in order to enable a rapid localization and quantification of all the dominant noise sources [2]. Phased array methods have been developed since the beginning of the Second World War, to optimize both the transmission and the reception of directional signals [3], while nowadays, they find their application in several fields, ranging from radio astronomy to medical imaging. The first example of an acoustic implementation dates back to 1974, when J. Billingsley developed an acoustic telescope to localize sound sources on full-size jet engines [4]. Since then, thanks to advancements in hardware systems, there has been a significant improvement in performance, allowing accurate studies of the sound fields generated by both stationary and moving sources, even in noisy environments.

Concerning the acquisition step, several optimization studies on microphone array geometries have been developed within the last few decades [5] [6] and, as computational power has steadily increased, higher sampling frequencies and sampling times can be set, thus ensuring remarkable advances in terms of sound sources discernment and spurious sources suppression. Nevertheless, due to the high cost of the entire acquisition equipment and the significant amount of data to be saved, the economic budget must always be considered. Regarding signal processing, instead, multiple algorithms have been developed, which can be broadly classified into two groups: time-domain methods and frequency-domain methods. Throughout the research, it will be possible to gain a thorough understanding of the theory underlying both implementations, when it is more convenient to focus on one over the other, and what their strengths and weaknesses are; in particular, the focus will be on sound sources investigation in rotating frameworks.

Nowadays moving sources are mostly approached with time-domain methods since they are able to seamlessly handle scenarios that change over time. However, multiple drawbacks have to be faced: the computational cost increases dramatically with the scanning grid definition and no advanced beamforming techniques, such as Generalized Inverse BeamForming (GIBF) [7], can be applied. On the other hand, frequency-domain methods are primarily used to investigate stationary sound sources, but they can significantly reduce the required time and offer the possibility to improve the source analysis through advanced techniques, stimulating the interest of many research institutes. In the year

2015, Herold and Sarradj [8] wrote an algorithm, based on the frequency-domain approach, able to deal with rotating sources and produce accurate results; however, its application is limited by geometrical bounds and requires the employment of a circular microphone array, turning out incompatible with many experimental setups. In the year 2020, Jekosch et al. [9] extended the capabilities of this algorithm, allowing the use of irregularly shaped microphone arrays, but relevant restrictions continue to limit the spread of such methods.

The goal of this work is to study the performance of the aforementioned algorithms and, when possible, optimize them in order to understand which limits can be overcome and which are strictly related to the method. Moreover, advanced deconvolution techniques in both the time- and frequency-domain are highlighted to further improve the acoustic source localization in the beamforming maps. The document is outlined as follows: Chapter 2 provides the theoretical background required to clearly understand the physics behind acoustic waves propagation; moreover, it offers an overview of the fundamental conventional beamforming techniques, introducing time-domain and frequency-domain approaches. Chapter 3 illustrates and deepens all of the most performant algorithms employed for the investigation of noise sources in rotating machines, introducing also the benchmarks and software used within the analysis. Chapter 4 displays and discusses all of the results achieved and, finally, chapter 5 draws the conclusions and suggests future perspectives.

Chapter 2

Theoretical background

In this chapter, starting from the Navier-Stokes equations and applying the appropriate hypothesis, the fundamental acoustic equations will be derived and their solution will be described, providing a strong mathematical basis to the topic.
Moreover, in the second section, the acoustic beamforming theory will be introduced and outlined in detail, beginning from the analysis of stationary sources up to focusing on more complex scenarios, such as moving sources and rotating frames.

2.1 Acoustic wave equation

In physics, sound consists of a weak pressure fluctuation that propagates through a transmission medium as an acoustic wave.
To derive the fundamental acoustic laws which govern the wave propagation, it is necessary to begin from Navier-Stokes equations, considering the proper assumptions. For a fluid in motion, considering the most general formulation in differential form, N-S can be written as follows:

$$\frac{\partial \rho}{\partial t} + \nabla \cdot (\rho \boldsymbol{u}) = Q_m \tag{2.1}$$

$$\rho\left(\tfrac{\partial \boldsymbol{u}}{\partial t} + \boldsymbol{u} \cdot \nabla \boldsymbol{u}\right) = -\nabla p + \nabla \cdot [\mu(\nabla \boldsymbol{u} + \nabla \boldsymbol{u}^{\boldsymbol{T}}) + \lambda(\nabla \cdot \boldsymbol{u})\boldsymbol{I}] \cdot \boldsymbol{u} + \rho \boldsymbol{f}_b \tag{2.2}$$

$$\rho\left(\frac{\partial E}{\partial t} + \boldsymbol{u}\cdot\nabla E\right) = -\nabla\cdot(p\boldsymbol{u}) + \nabla\cdot\{[\mu(\nabla\boldsymbol{u} + \nabla\boldsymbol{u}^{\boldsymbol{T}}) + \lambda(\nabla\cdot\boldsymbol{u})\boldsymbol{I}]\cdot\boldsymbol{u}\} \\ +\nabla\cdot(\nabla T) + \rho\boldsymbol{f}_b\cdot\boldsymbol{u} + Q_W. \tag{2.3}$$

Eq. (2.1) is the continuity equation and studies the balance between mass variation and the presence of mass sources Q_m; eq. (2.2) is the momentum equation and states the momentum trend as a function of pressure gradients, viscous effects, and body forces; eq. (2.3), finally, is the energy equation and describes the energy loss/gain due to pressure and temperature gradients, viscous stresses, body forces, and heat sources Q_W.

Assuming that the effect of fluid viscosity and thermal conductivity terms could be neglected, this set of equations can be simplified. This operation leads to Euler equations:

$$\frac{\partial\rho}{\partial t} + \rho\nabla\cdot\boldsymbol{u} + \boldsymbol{u}\cdot\nabla\rho = Q_m \tag{2.4}$$

$$\rho\left(\frac{\partial\boldsymbol{u}}{\partial t} + \boldsymbol{u}\cdot\nabla\boldsymbol{u}\right) = -\nabla p + \rho\boldsymbol{f}_b \tag{2.5}$$

$$\rho T\left(\frac{\partial s}{\partial t} + \boldsymbol{u}\cdot\nabla s\right) = Q_W. \tag{2.6}$$

In the latter case, the energy equation is written as a function of the entropy s.
Since the objective of the treatment is to obtain a set of equations that let us study acoustic phenomena, further approximations can be carried out. Assuming that the propagation medium is characterized by no significant flow and that it is possible to define each fluid dynamic variable as the sum of a constant value $(.)_0$ plus a perturbation induced by the sound wave $(.)'$, with $(.)'/(.)_0 << 1$:

$$\begin{aligned}\rho(\mathbf{x},t) &= \rho_0 + \rho'(\mathbf{x},t)\\ p(\mathbf{x},t) &= p_0 + p'(\mathbf{x},t)\\ \boldsymbol{u}(\mathbf{x},t) &= \boldsymbol{u}_0 + \boldsymbol{u}'(\mathbf{x},t) = \boldsymbol{u}'(\mathbf{x},t).\end{aligned} \tag{2.7}$$

Substituting the equations (2.7) within Euler equations and neglecting high order terms, it is possible to achieve the linearized Euler equations:

$$\frac{\partial \rho^{'}}{\partial t} + \rho_0 \nabla \cdot \boldsymbol{u}^{'} = Q_m \tag{2.8}$$

$$\rho_0 \frac{\partial \boldsymbol{u}^{'}}{\partial t} = -\nabla p^{'} + \rho_0 \boldsymbol{f}_b \tag{2.9}$$

$$\rho_0 T_0 \frac{\partial s^{'}}{\partial t} = Q_W. \tag{2.10}$$

The proper combination of this last set of equations will lead to the attainment of the wave equation in a homogeneous medium: the first step consists of subtracting the divergence of the momentum equation (2.9) from the time derivative of the mass conservation one (2.8). This operation will converge in the following formula:

$$\frac{\partial^2 \rho^{'}}{\partial t^2} - \nabla^2 p^{'} = \frac{\partial Q_m}{\partial t} - \rho_0 \nabla \cdot \boldsymbol{f}_b. \tag{2.11}$$

Since density variations are difficult to be investigated, to study acoustic waves, it is desirable to derive a formula in function of the pressure perturbation. To meet such need, it is possible to introduce the constitutive equation, which links $p^{'}$, $\rho^{'}$ and $s^{'}$:

$$dp^{'} = {c_0}^2 d\rho^{'} + \frac{p_0}{c_v} ds^{'}. \tag{2.12}$$

A further combination of (2.11), (2.12) and (2.10) is necessary to obtain the in-homogeneous wave equation:

$$\frac{1}{{c_0}^2} \frac{\partial^2 p^{'}}{\partial t^2} - \nabla^2 p^{'} = \frac{\partial}{\partial t} \left(Q_m + \frac{\gamma - 1}{2} Q_W \right) - \rho_0 \nabla \cdot \boldsymbol{f}_b. \tag{2.13}$$

Eq. (2.13) provides the effective pressure variation due to the sound propagation. Its left-hand term consists of the D'Alembertian operator applied to the pressure perturbation p', while its right-hand term contains the sound sources: in the most general case, the propagation of acoustic waves is due to the unsteady injection of mass sources $\frac{\partial Q_m}{\partial t}$ and heat sources $\frac{\partial Q_W}{\partial t}$, and the fluctuation of force fields $\boldsymbol{f}_b$. Different sound sources generate

different wave propagation mechanisms, indeed, the terms $\frac{\partial Q_m}{\partial t}$ and $\frac{\partial Q_W}{\partial t}$ are associated with an acoustic monopole, while the term $\nabla \cdot \boldsymbol{f}_b$ is associated to an acoustic dipole. Moreover, if viscous phenomena are not ignored, eq. (2.13) includes the contribution of non-uniform viscous stresses which produce quadrupole acoustic sources. To provide a better understanding of how monopoles, dipoles, and quadrupoles propagate, their directivity pattern is represented in fig. 2.1.

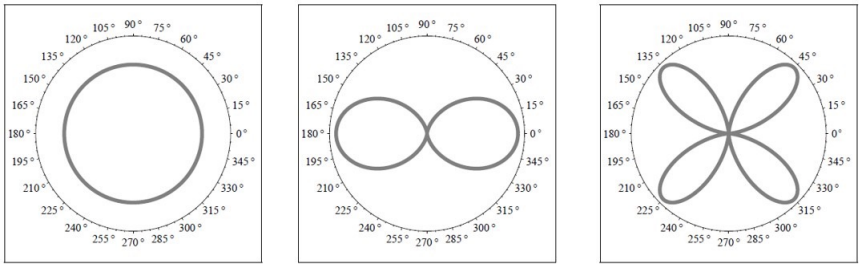

Figure 2.1: Directivity pattern of a monopole, a dipole and a quadrupole [2].

It has previously been demonstrated that sound can be studied as a pressure perturbation that travels as a wave through a fluid medium. When compared to the mean environmental pressure, the amplitude of its fluctuation is negligible, but it can cover a very wide range; for example, the acoustic pressure at the pain threshold is approximately ten million times higher than the one at the hearing threshold. Since it is necessary to work with very different orders of magnitude, it is convenient to introduce a logarithmic scale.
Thus, it is possible to define the *Sound Pressure Level* (SPL) as:

$$SPL\ [dB] = 20 \cdot log\left(\frac{p_{rms}}{p_{ref}}\right) \tag{2.14}$$

where p_{rms} is the root mean square of the pressure signal and p_{ref} is the reference pressure ($2 \cdot 10^{-5}$ Pa if the air is the medium in which waves propagate).
The human ear can detect SPL in the range of 0 dB, which corresponds to barely audible sound perturbation, to 130 dB, which corresponds to painful noise.

2.2 Conventional beamforming techniques

The primary responsibility of acoustical engineers is to control and improve the sound environment in which people work. As a result, aeroacoustic measurements are always designed with the goal of determining the precise location of sound sources and their relative intensity. The most widely used techniques today are based on the acoustic source mapping theory and can provide accurate results in both noisy environments and moving frameworks. Such outcomes require a preliminary acquisition step: the experimental setup is usually arranged in an anechoic wind tunnel to reduce the effect of background noise and the pressure data are extrapolated by a certain number of microphones, all installed on a properly tailored physical support.
In this section, conventional beamforming techniques for stationary sources will be described, as well as their extension for moving frameworks, in order to provide the detailed background required to understand the algorithms presented in Chapter 3.

2.2.1 Time-domain conventional beamforming

The most common manner to identify acoustic sources with a phased array of microphones is conventional beamforming [10] and it can be implemented either in time- or frequency-domain. Both methods will be explained in the following lines, along with a more general assessment of their strengths and weaknesses.
The analysis starts from time-domain conventional beamforming, which has its principles in the delay & sum algorithm, well summarized in fig. 2.2. Its comprehension can be broken down into four major steps:

- Firstly, let‘s consider far-field conditions and, hence, plane wavefronts. This assumption is valid if the distance between the microphone array and the source is several orders of magnitudes greater than the wavelength of the acoustic signal.
- The target wavefront reaches each sensor at different times. Considering a very simple array geometry as the one shown in fig. 2.3, the time delay t_d can be estimated by using the eq. (2.15), where d is the distance between two microphones, c_0 is the sound propagation speed at the measurement conditions and θ is the angle between the microphone axis and the normal to the wavefront.

$$t_d = \frac{d\ cos\theta}{c_0}. \tag{2.15}$$

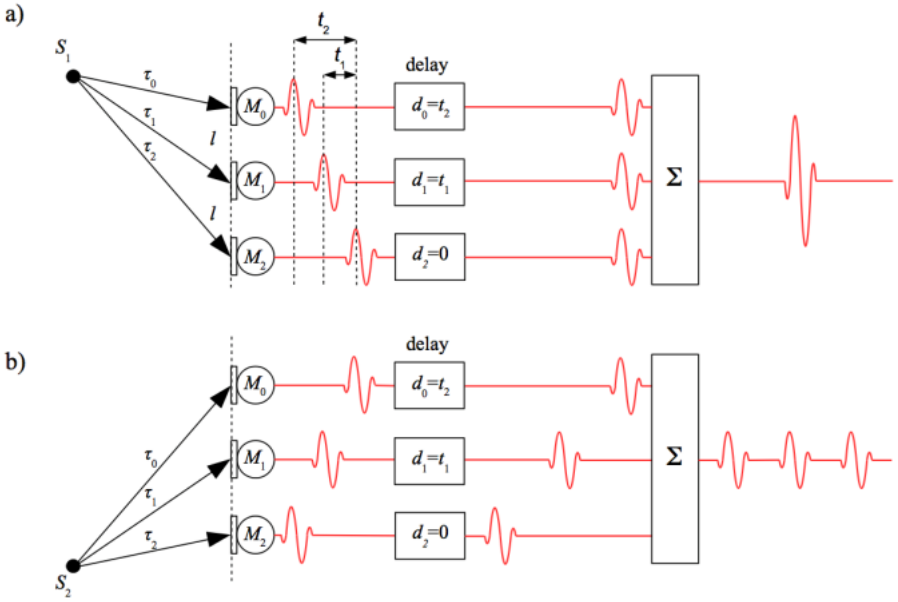

Figure 2.2: Delay & sum scheme with a three microphones array.

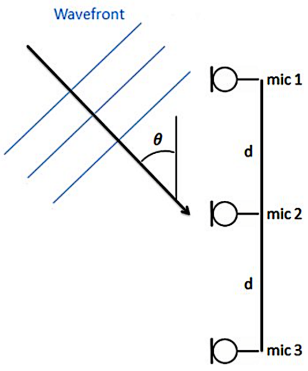

Figure 2.3: Schematic representation of a plane wave reaching a three microphones array.

- Depending on the focus point, according to the above-mentioned time delay relation, the information extrapolated by the sensors is shifted.
- Finally, all the signal components are summed up and, as a function of the number of the microphones, a further normalization is applied. This operation gives us an idea of both the source sound level and position.

By taking a look at eq. (2.15), since d is fixed and c_0 only depends on the environmental conditions, modifying t_d it is possible to numerically steer the antenna and, hence, to analyze a wide area without moving the instrumentation. The output obtained by using

this algorithm is the pressure level in function of the angle θ and its maximum value corresponds to the dominant sound source in the monitoring area. Fig. 2.4 shows the output of a single point source emitting 94 dB, with an incident angle of 45°.

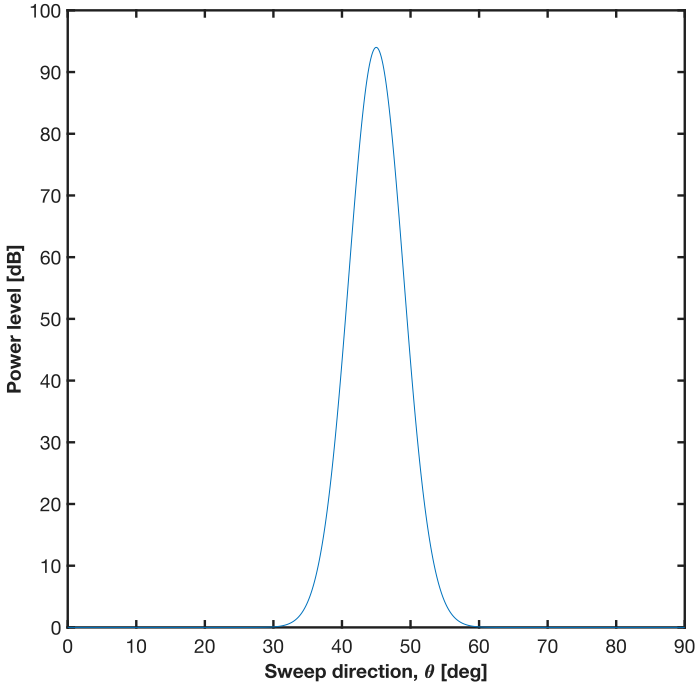

Figure 2.4: Intensity of the wavefront in relationship to the sweep angle.

2.2.2 Frequency domain conventional beamforming

When considering frequency-domain conventional beamforming, a different approach is taken. Assuming that the acquisition system consists of N microphones that acquire samples at a fixed sampling frequency f_s, for a given sampling time t_s, each sensor will provide a K-dimensional vector of recorded pressures $\boldsymbol{p}(t)$, where $K = t_s \cdot f_s$. The use of the Fourier transform allows the transition from the time-domain to the frequency-domain, so $\boldsymbol{p}(t)$ becomes $\boldsymbol{p}(f)$, while retaining the former dimension:

$$\boldsymbol{p}(f) = \begin{pmatrix} p_1(f) \\ \vdots \\ p_N(f) \end{pmatrix} \tag{2.16}$$

where $p_i(f) \in C$.
Assuming a scanning grid of j points and considering a single point source located in the scan point ζ_j, the received signal is defined as $s_j \boldsymbol{g}_j$; where s_j is the source intensity and $\boldsymbol{g}_j \in C^{N\text{x}1}$ is the steering vector [11]. The shape of the steering vector depends on the source type, on environmental conditions, on the grid scan point ζ_j and on the desirable properties which have to be investigated. Several definitions have been formulated and a more detailed overview is provided by Sarradj [12].
Taking into account a stationary monopole source for simplicity, it is possible to state that the steering vector primarly contains the free-field Green's function of the Helmholtz equation [11]:

$$g_{j,n} = \frac{e^{(-2\pi i f \Delta t_{j,n})}}{4\pi \left\| x_n - \zeta_j \right\|} = \frac{e^{(\frac{-2\pi i f \|x_n - \zeta_j\|}{c_0})}}{4\pi \|x_n - \zeta_j\|} \tag{2.17}$$

where the term $\Delta t_{j,n}$ indicates the time delay between the sound perturbation emission from a point ζ_j and the reception by a sensor located in $\boldsymbol{x}_n = (x_n, y_n, z_n)$.
An estimation of the beamforming output can be given by the following formula:

$$CB(\zeta_j) = \frac{1}{2} \frac{\boldsymbol{g}_j{}^* \langle \boldsymbol{p}\boldsymbol{p}^* \rangle \boldsymbol{g}_j}{\|\boldsymbol{g}_j\|^4} = \boldsymbol{w}_j{}^* \boldsymbol{CSM} \boldsymbol{w}_j. \tag{2.18}$$

The operators $(.)^*$ and $\langle . \rangle$ respectively denote the complex conjugate transpose and the time average taken over several snapshots; the vector $\boldsymbol{w}_j$ is the weighted steering vector and $\boldsymbol{CSM} \in C^{N\text{x}N}$ is the cross-spectral matrix. Eq. (2.18) is computed for each focus point of the grid, thus obtaining the beamforming map for a given frequency band.

Once an overall view of both methods is given, it is possible to illustrate their principal strengths and weaknesses. Time-domain conventional beamforming performs better when dealing with moving sources, but it requires more computational time as the number of grid elements increases [10]. On the other hand, frequency-domain conventional beamforming produces optimal results while analyzing stationary sources, but, cannot deal with moving sources without further advancement.
Both the methods are strictly dependent on the inspected signal frequency. At low frequencies the acoustic signal beamwidth is considerable and the presence of side lobes is negligible (fig. 2.5 a), hence, the beamforming map will appear blurred and just the main lobe will be noticed. At high frequencies, instead, the beam becomes narrow, but

the sidelobe ratio decreases significantly (fig. 2.5 b) spoiling the beamforming map with spurious sources [13].

(a) (b)

Figure 2.5: (a) Beam shape at low frequencies. (b) Beam shape at high frequencies.

2.2.3 The Point Spread Function (PSF)

While analyzing the drawbacks of conventional beamforming techniques, the issue of spatial resolution (especially at low frequencies) and the presence of sidelobes was highlighted (especially at high frequencies). Ideally, the beamforming map generated by point sources should show only infinitesimally narrow dots emitting at the exact expected SPL, with no other spurious sources present. However, due to the finite size of the microphone array and the discontinuous distribution of microphones, any real microphone array will spatially alias the point source and contaminate the beamforming output map with sidelobes, which are referred to as "pseudo" sound sources [14].
In acoustics, the impulse response of an array to a unitary amplitude point source is known as the point spread function (PSF) [15], and actual conventional beamforming results are the convolution of real patterns and the PSF of the microphone array used in the experiments.
In order to provide a quantitative evaluation of microphone array performances, two main parameters were defined: the beamwidth and the dynamic range. The first parameter measures the spatial resolution and consists of the main lobe diameter 3 dB below the peak SPL value, whereas the latter evaluates how spoiled the beamforming map is, due to the presence of spurious sources. This latter value is referred to as the sidelobe ratio, and it estimates the difference between the main lobe peak value and the highest sidelobe SPL (fig. 2.6). Several studies have been conducted to optimize the microphone array geometry, which were well summarized by Sarradj [5] and will not be expanded upon in this research.

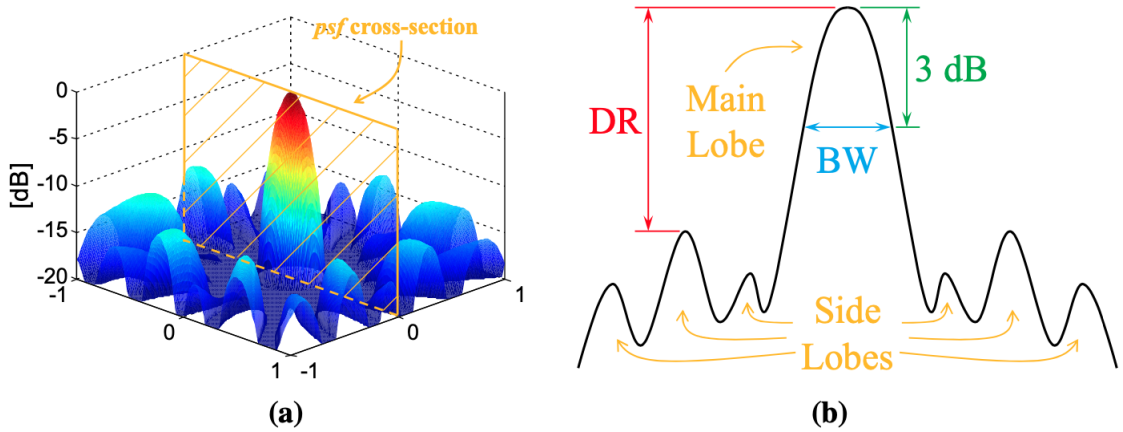

Figure 2.6: Schematic representation of the beamwidth and the dynamic range. (a) 3D PSF. (b) 2D PSF.

2.2.4 Moving sources

Up to now, two basic beamforming techniques have been described, both of which can provide adequate results only if stationary sources have to be identified. Microphone arrays methods, however, are powerful tools and also offer the opportunity to locate sources on moving objects. This application, which is still in its early stages, has been tested on trains passing by [16], on airplanes flyover [17] and further test cases.
This section will explain in detail how sound perception changes depending on the relative speed of the acoustic source and the receiver. All of the calculus will converge in the so-called *Doppler frequency shift* and *Doppler amplification*, which must be considered when performing the beamforming process.

In section 2.1, the in-homogeneous wave equation was achieved (2.13), starting from the N-S equations and introducing the proper assumptions.
To make explicit its solution, the Green's function method can be employed: the acoustic field $G(\mathbf{x}, t)$ related to an impulsive source, emitted at position $\mathbf{y}$ and time τ is given by the formula:

$$\frac{1}{{c_0}^2}\frac{\partial^2 G}{\partial t^2} - \nabla^2 G = \delta(\mathbf{x}-\mathbf{y})\delta(t-\tau) \tag{2.19}$$

where δ consists of the Dirac delta and $\mathbf{x}$ is the receiver position. By ignoring the effect of dipoles and quadrupoles, grouping all the monopolar acoustic sources in the term $q(\mathbf{x}, \tau)$ and applying Green's theorem, the solution of eq. (2.13) becomes [18]:

$$p(\mathbf{x}, t) = \int_{-\infty}^{t}\int_{V} q(\mathbf{y}, \tau) G\langle \mathbf{x}, t|\mathbf{y}, \tau\rangle d^3\mathbf{y}d\tau - \int_{-\infty}^{t}\int_{S}\left(p\frac{\partial G}{\partial y_i} - G\frac{\partial p}{\partial y_i}\right)n_i d^2\mathbf{y}d\tau. \tag{2.20}$$

Assuming free space conditions, the Green's function can be written as:

$$G_0\langle \mathbf{x}, t|\mathbf{y}, \tau\rangle = \frac{\delta(t-\tau-\|\mathbf{x}-\mathbf{y}\|/c_0)}{4\pi\|\mathbf{x}-\mathbf{y}\|}. \tag{2.21}$$

Hence, it follows that:

$$p(\mathbf{x}, t) = \int_{-\infty}^{t}\int_{V}\frac{q(\mathbf{y}, \tau)}{4\pi\|\mathbf{x}-\mathbf{y}\|}\delta(t-\tau-\|\mathbf{x}-\mathbf{y}\|/c_0)d^3\mathbf{y}d\tau. \tag{2.22}$$

For a moving point source at position $\zeta(\tau)$, which emits a signal $\sigma(\tau)$, it is possible to express the term $q(\mathbf{y}, \tau)$ as:

$$q(\mathbf{y}, \tau) = \sigma(\tau)\delta(\mathbf{y} - \zeta(\tau)). \tag{2.23}$$

Substituting eq. (2.23) into (2.22) and defining the term $r^{'} = \|\mathbf{x} - \zeta(\tau)\|$ (which consists of the distance between source and receiver at the emission time), it will follow that:

$$p(\mathbf{x}, t) = \int_{-\infty}^{t} \frac{\sigma(\tau)\delta(t - \tau - r^{'}/c_0)}{4\pi r^{'}} d\tau. \tag{2.24}$$

Operating a change of variables, eq. (2.24) can be written as:

$$p(\mathbf{x}, t) = \int_{-\infty}^{\infty} h(\tau)\delta(g(\tau))d\tau. \tag{2.25}$$

And for discrete times, it follows that:

$$p(\mathbf{x}, t) = \sum_{n=1}^{N} \frac{h(\tau_n)}{|dg/d\tau|_{\tau=\tau_n}} \tag{2.26}$$

where τ_n are the zeros of the function $g(\tau) = 0$.
The denominator term is the time derivative of the distance $r^{'}$, which is equal to the relative speed multiplied by the cosine of the θ angle (angle between the source direction and the source-receiver one, both at the emission time).
For subsonic speeds, it will follow that:

$$p(\mathbf{x}, t) = \frac{\sigma(\tau_n)}{4\pi r^{'}(1 - Mcos\theta)} \tag{2.27}$$

where M is the source Mach number.
The factor $(1 - Mcos\theta)^{-1}$ is called *Doppler amplification* and corrects the acoustic signal amplitude. In the same way, the perceived frequency differs from the source one, hence, a further correction has to be applied. By defining as f the source signal frequency, it is possible to state that each microphone will measure a frequency $fd\tau_n/dt$. Since $\tau_n = t - r^{'}/c_0$, it follows that:

$$fd\tau_n/dt = \frac{f}{1 - Mcos\theta}. \tag{2.28}$$

This factor is known as *Doppler frequency shift* and helps us to understand that when the acoustic source moves towards the observer, the perceived frequency is higher ($cos\theta > 0$).

Chapter 3

Methodology

In this chapter, the most efficient beamforming algorithms for rotating sources are explained in detail; their principal strengths and weaknesses are presented and an overview of some powerful deconvolution methods is given.
The first sections cover frequency-domain beamforming techniques that make use of the VRAM signal processing algorithm and its extension for irregularly shaped microphone arrays. Furthermore, the Clean and Clean-SC methods will be introduced, highlighting the strengths of the deconvolution methods. Following that, the emphasis shifts to time-domain approaches such as ROSI and Clean-T and, at last, the software Acoular, the synthetic and the experimental test cases are detailed.
All the validation process outcomes and an experimental analysis, completed using the aforementioned techniques, will be outlined in Chapter 4.

3.1 Virtual Rotating Array Method (VRAM)

Nowadays, time-domain beamforming is the most commonly used method for analyzing the characteristics of noise sources in moving objects, but even if the results are accurate enough and the beamforming maps are very clear, the computational cost is significant and grows with the number of grid elements. In order to reduce the time required to process the acquired data, modern researchers are focusing their efforts on developing frequency-domain algorithms capable of dealing with moving sources.
Herold and Sarradj have developed a computer program called VRAM (Virtual Rotating Array Method) [8], able to satisfy the above-mentioned need for certain test case symmetries: by taking advantage of the rotating frame characteristics, employing a ring-shaped array

(fig. 3.1), it is possible to pre-process the gathered data to simulate a rotation of the acquiring system at the sources angular rate. As a result, there will be no relative speed between the sources and the microphone array, allowing standard frequency-domain algorithms to be used. Nonetheless, the virtual signals obtained mostly correspond to positions where no microphones are installed; the sound pressures at these positions are thus computed by interpolating between the values detected by adjacent sensors. All additional information needed to fully comprehend how VRAM works are provided in the following lines.
Before delving into the algorithm's details, it's important to note that its outcomes are strictly linked to a few constraints:

- The microphone array has to be circular.
- The rotational axis of both the virtual array and the inspected machine have to be aligned.
- The angular speed of both the virtual array and the inspected machine have to be equal and slightly constant.

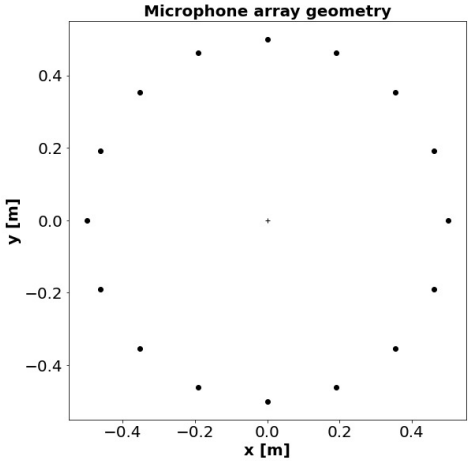

Figure 3.1: Ring array with 16 microphones.

After a brief introduction, let's move forward explaining how VRAM works. In a circular array of N equally spaced microphones, it is possible to define the angular distance between each of them, as:

$$\alpha = \frac{2\pi}{N}. \tag{3.1}$$

Since the virtual rotation is rigid, α doesn't change. Nevertheless, after a certain amount

of time Δt, the virtual microphones rotate by an angle $\Delta\varphi$ (fig. 3.2), thus, a vector $\varphi(t)$ can be defined, containing the exact angular position of the virtual microphone array at each instant.
Once $\varphi(t)$ is clearly determined, denoting with n the index of a generic virtual rotating microphone, it is possible to find the indices of the two real ones (n_l and n_r), which will be thereafter employed within the interpolation process:

$$\begin{aligned} n_l(n,t) &= \left\lfloor n + \frac{\varphi(t)}{\alpha} - 1 \right\rfloor mod N + 1 \\ n_r(n,t) &= \left\lfloor n + \frac{\varphi(t)}{\alpha} \right\rfloor mod N + 1. \end{aligned} \tag{3.2}$$

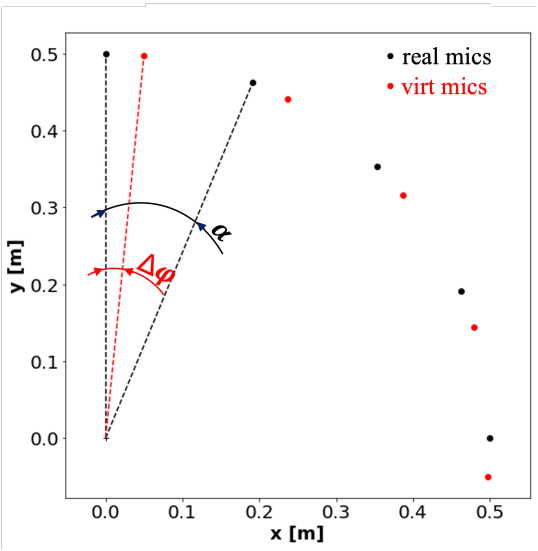

Figure 3.2: Virtual microphones positions after a time Δt.

At the same time, knowing the virtual rotating array exact position, enables the possibility to compute the weighting factors (s_l and s_r) which have to be introduced in the linear equation:

$$\begin{aligned} s_l(t) &= \frac{\varphi(t)}{\alpha} - \left\lfloor \frac{\varphi(t)}{\alpha} \right\rfloor \\ s_r(t) &= 1 - s_l(t). \end{aligned} \tag{3.3}$$

All the steps that have been executed up to now converge in the linear interpolation formula:

$$p_{vr,n}(t) = s_l(t)p_{n,l}(t) + s_r(t)p_{n,r}(t). \tag{3.4}$$

The resulting matrix $p_{vr,n}(t)$ contains the pressure signals that the sensors would have acquired if the microphone array had rotated at the same speed as the inspected object. It is important to note that non-constant angular speeds have no effect on the precision of such calculus; however, the above-described process inevitably conceals errors due to the linearization of a non-linear phenomenon, such as wave propagation in a fluid medium. The magnitude of such errors is strictly proportional to the inspected frequency, increasing as the focus shifts to higher frequencies.

Once all the interpolated sound pressures have been computed, the CSM for the rotating framework can be obtained, in the same way that the CSM for a stationary case would have been. Before determining the acoustic beamforming map, a further correction must be applied: the steering vectors, which describe the sound propagation from a generic focus point to a generic microphone, must take into account the reference system rotation. The scheme of a microphone array measurement for rotating source identification is depicted in fig. 3.3 At the time of emission, the sound source, denoted by the letter P, emits an acoustic wave that propagates towards the acquiring system; even if both the source and the virtual microphones rotate at the same speed, the time delay between signal emission and reception must be considered when calculating the propagation distance. Indeed, due to the rotation, the pressure signal will be gathered by a virtual microphone located in position N' rather than one located in position N, and thus, in order to define the correct steering vector, the distance r'_{np} must be estimated iteratively.

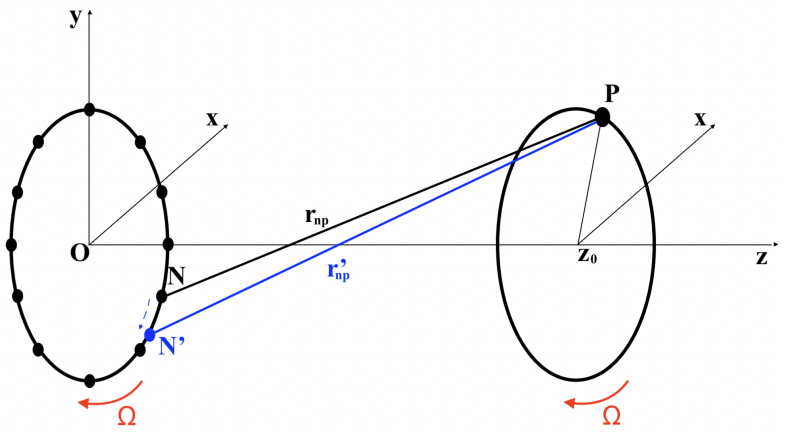

Figure 3.3: Scheme of the microphone array measurement.

Unfortunately, this last correction conceals considerable issues when dealing with variable rotational rates. When switching from the time-domain to the frequency-domain, the time history of the microphone positions cannot be used, preventing the algorithm from adjusting speed fluctuations. As a result, precise steering vectors can only be provided when the inspected device, and thus the virtual array, rotates at a constant angular rate. However, as will be demonstrated later, if speed fluctuations are not significant, the error can be ignored. After defining the cross-spectral matrix and steering vectors, the beamforming map can be generated using the same formula used for the stationary case.

3.2 VRAM for irregularly shaped microphone array

The Virtual Rotating Array Method can deliver impressive results in terms of beamforming map quality and computational cost. However, before an experimental campaign begins, a few drawbacks must be considered: the microphone array shape must be circular, and the virtual microphone array center of rotation must be aligned with the rotational axis of the inspected object.
Within the last years of research on frequency-domain algorithms, further VRAM extensions have been provided. Jekosch et al. [9] elaborated two methods based on interpolation processes over irregular microphones layouts: one uses radial basis function approximations and the other uses the Delaunay triangulation to define a triangular mesh. Such algorithms enable the use of irregularly shaped microphone arrays, but they do not address the constraint of aligning both rotational axes. Based on Jekosch results, the mesh-based algorithm performs better in terms of source localization quality and computational cost; thus, the following lines will provide a more detailed explanation of the logical steps it goes through. Furthermore, as part of the Training Programme at the von Karman Institute, a further enhancement was implemented to improve mesh definition.

Jekosch's Virtual Rotating Array Method extension can be briefly summed up by the flowchart reported in fig. 3.4. The algorithm requires three inputs: K signals acquired by the tachometer, KxN pressure signals acquired by the microphones and the array geometry. Moreover, in order to simplify the interpolation process, the reference system is changed from a cartesian (fig. 3.5) to a cylindrical one (fig. 3.6): in the latter framework, the virtual rotation can be seen as a translation of the microphones along the φ-axis.

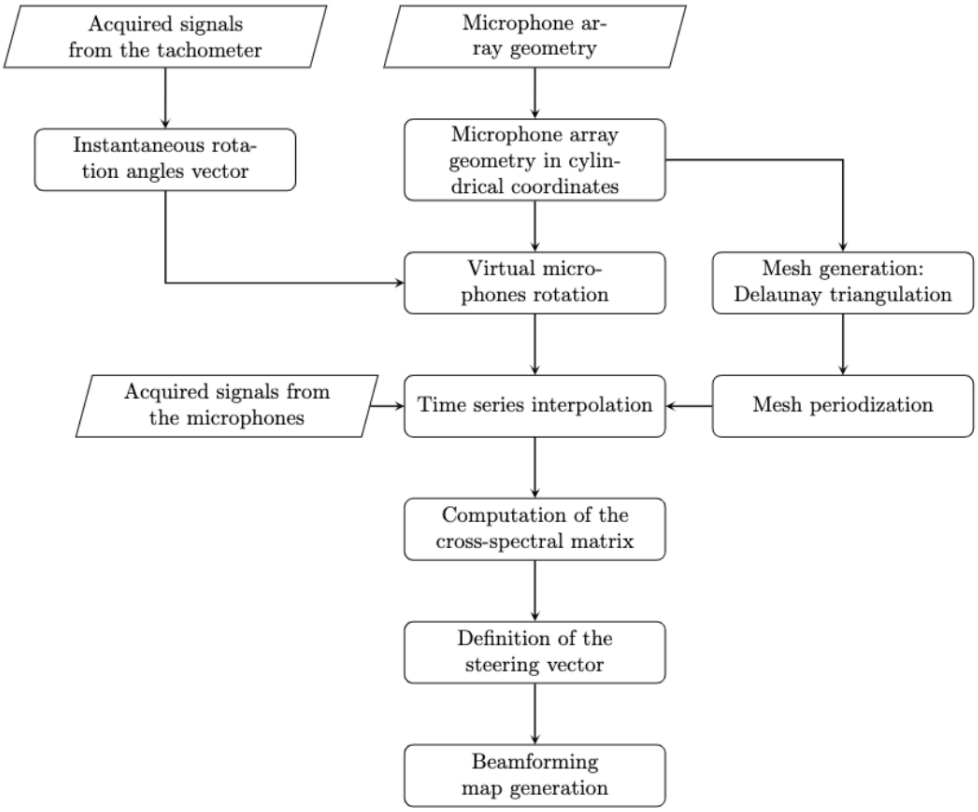

Figure 3.4: Flowchart of the VRAM extension provided by Jekosch [9].

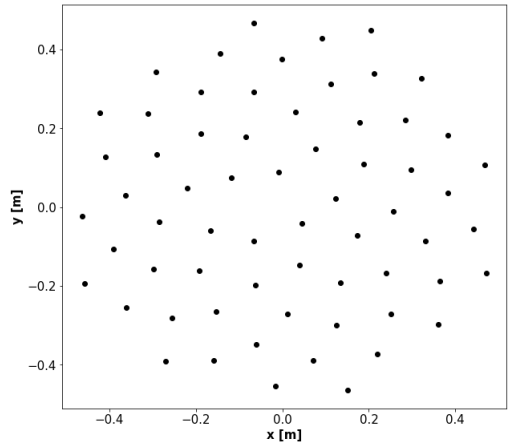

Figure 3.5: Microphone array cartesian layout.

To comply with the angular periodicity and cover the entire domain with the mesh, before applying the Delaunay triangulator, some microphone positions must be added to the left and right, repeated in the angular direction (fig. 3.7). Following this step, the mesh

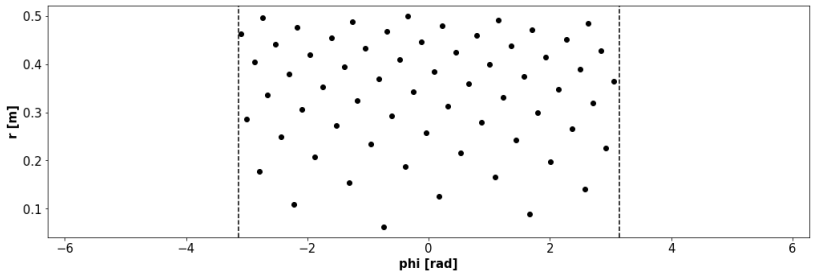

Figure 3.6: Microphone array cylindrical layout.

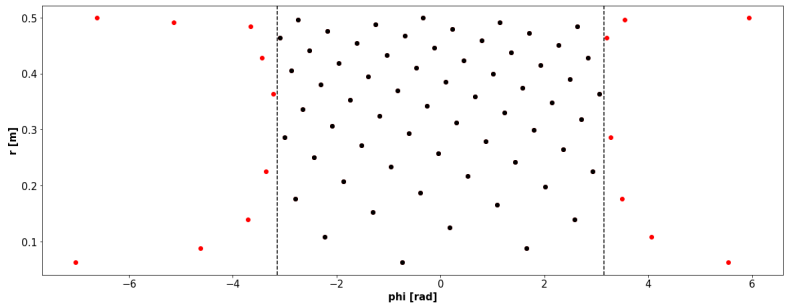

Figure 3.7: Microphone array extension to comply with the virtual rotation.

generated by Delaunay triangulation (fig. 3.8), the time series of pressure signals acquired by the microphones and the virtual microphones positions at each sampling instant can be combined to provide the interpolated time series of the acoustic pressures. As previously stated for conventional VRAM, such a result consists of the pressure signals gathered by the sensors if the microphone array rotated at the source angular speed.
Once the virtual time series is available, the beamforming process coincides with the conventional one.

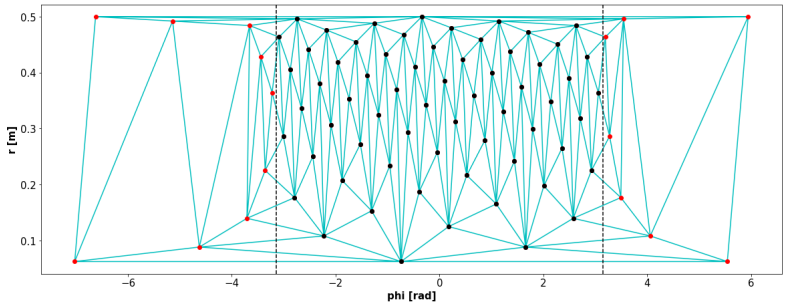

Figure 3.8: Delaunay triangulation in cylindrical coordinates.

The previously described process reveals an inconsistency in the mesh definition: the interpolation occurs between microphones that are close in the cylindrical reference system, whereas the real-time series is acquired in the cartesian one. To avoid this problem, a slightly different algorithm was developed and summarized in the flowchart shown in fig. 3.9.

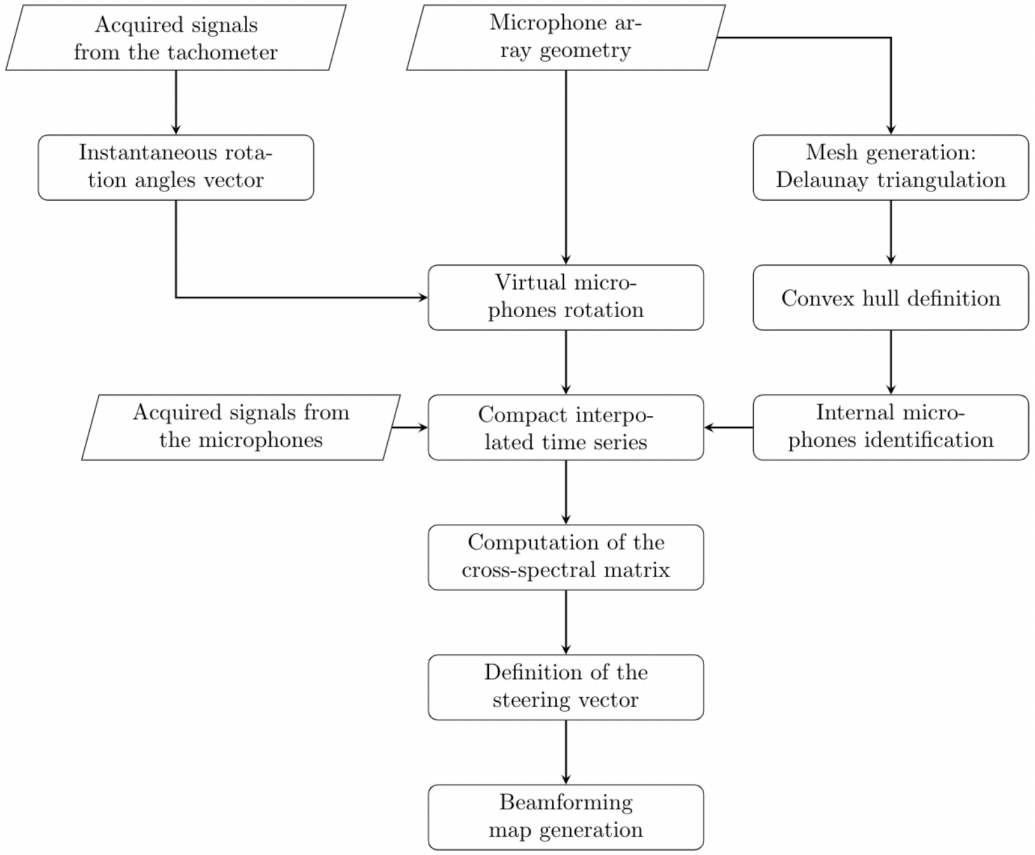

Figure 3.9: Flowchart of the modified VRAM extension.

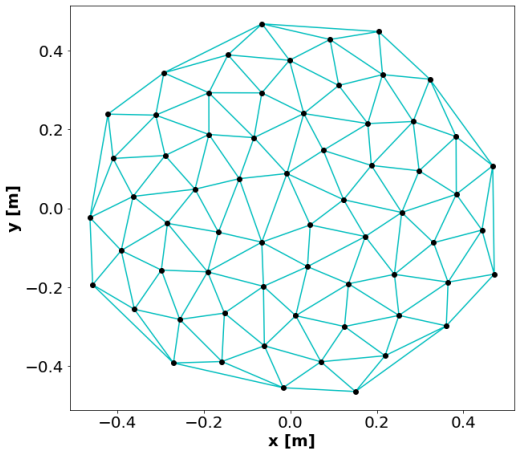

Figure 3.10: Delaunay triangulation in cartesian coordinates.

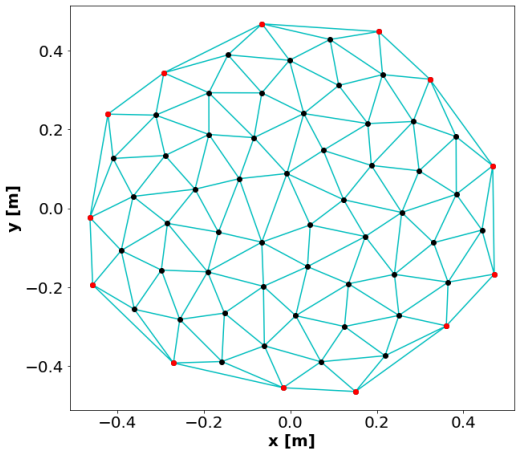

Figure 3.11: Delaunay triangulation in cartesian coordinates. The red points are not considered in the CSM definition.

The overall process is the same as reported earlier, but the mesh is defined directly in the cartesian reference system (fig. 3.10). This step improves the interpolated signal's reliability, but it introduces a new issue: when the virtual array rotates, the nodes at the edge go out of the mesh.
To avoid inconsistencies, just the internal microphones are involved in the cross-spectral-matrix definition (black points in fig. 3.11). The outcome of this trade-off shows better performances.

3.3 Frequency-domain deconvolution algorithms

Deconvolution methods have sparked interest in the acoustic community because they provide the opportunity to improve array resolution while reducing unwanted sidelobe effects [19]. Various methods, both in the time- and frequency-domain, have been implemented over the last few years. In this chapter, the emphasis will be on frequency-domain methods, with two of the most efficient algorithms described: Clean and Clean-SC.

Dougherty [20] was the first to use the Clean algorithm in acoustical measurement at the end of the last century, but the concept behind this technique had already been used in radio astronomy and remote sensing a few decades before.
It aims to suppress sidelobes by iteratively updating a "clean" map from a "dirty" one obtained through conventional beamforming techniques. The overall process can be summarized in a few paragraphs:

1. Frequency-domain conventional beamforming is firstly performed to compute the so-called "dirty map".
2. The "dirty map" is analyzed to identify the source peak level and, hence, the dominant source location.
3. Once the peak is known, the theoretical point spread function for a source at that level and position is computed.
4. The "dirty map" is updated by subtracting from it a fraction of such point spread function.
5. The "clean map" is updated by adding a fraction of the peak level.
6. Steps 2-5 are repeated iteratively until a stopping criterion is reached.

The Clean method is robust, but its performance is limited to simple test cases due to its fundamental assumptions: the deconvolution is fully related to the synthetic point spread function, which does not always mirror the dominant source beam pattern, and the acoustic field is treated as a superposition of point sources. Such hypotheses are no longer valid when studying coherent or distributed sources, as well as when the directivity patterns of the sources are non-uniform.

To overcome most of the aforementioned issues Sijtsma [21] implemented the Clean-SC algorithm. This deconvolution method is an extension of the previous one that considers the spatial coherence between the source main lobe and its sidelobes: by removing the

latter contributions, it is possible to significantly increase the sidelobe ratio and thus "clean" the beamforming map in a more consistent manner.
As for Clean, to achieve this result, the algorithm operates iteratively by following a similar scheme:

1. The "dirty map" is defined by executing conventional beamforming methods.
2. The peak level and location are identified in the "dirty map".
3. The contribution of spatially coherent sources (taking into account a gain factor γ) is subtracted from the "dirty map".
4. Coherent source signals are replaced by a "clean" beam and saved in the so-called "clean map".
5. Steps 2-4 are iterated until a stopping criterion is reached.

3.4 ROtating Sources Identifier (ROSI)

Frequency-domain methods can provide very satisfactory results while consuming less computational time; however, their application is limited by an intrinsic restriction: the source rotational axis and the virtual rotating array center must be perfectly aligned. Since they are not constrained by any geometrical limit, time-domain algorithms are commonly used to investigate moving sources. The theory underlying time-domain array measurements on moving objects is similar to that described for stationary sources, but some corrections must be made to account for the Doppler effect. Sijtsma and Oerlemans [22] have developed ROSI (ROtating Source Identifier) a software capable of dealing with rotating sources. According to the studies they have published, a brief review of the ROSI algorithm will be provided in the following lines.

In section 2.2.3 the pressure field generated by a monopolar source was derived (2.24), expressing the acoustic pressure perceived by a sensor at position $\mathbf{x}$, at a certain time t, as the product of the source signal at the emission time τ, the Doppler amplification and a factor dependent on the distance between the receiver and the source position at the emission time. From now on, all the factors that multiply the source signal will be grouped in the transfer function $H(\mathbf{x}, \zeta(\tau), t, \tau)$, thus obtaining:

$$p(\mathbf{x}, t) = H(\mathbf{x}, \zeta(\tau), t, \tau)\sigma(\tau). \tag{3.5}$$

Eq.(3.5) describes the theoretical acoustic signal a microphone at position $\mathbf{x}$ would acquire if no noise is considered. In reality, at each sampling time t_k, each microphone output can be written as:

$$p_n(\mathbf{x}, t_k) = H(\mathbf{x}_n, \zeta(\tau), t_k, \tau)\sigma_k + \varepsilon_n(t_k) \tag{3.6}$$

where $\varepsilon_n(t_k)$ denotes the noise emitted by other sources at the microphone-dependent receiver time t_k. According to Oerlemans [22], t_k can be made expressed explicitly as follows:

$$t_k = \tau - \frac{M\Big(\mathbf{x}_n - \zeta(\tau)\Big) \cdot \boldsymbol{e}_x}{1 - M^2} + \frac{\sqrt{M^2\Big\{\Big(\mathbf{x}_n - \zeta(\tau)\Big) \cdot \boldsymbol{e}_x\Big\} + \Big(1 - M^2\Big)\| \cdot \mathbf{x}_n - \zeta(\tau)\|^2}}{1 - M^2}. \tag{3.7}$$

Applying the Delay & Sum algorithm and neglecting the noise contribution, the final reconstructed source signal $\tilde{\sigma}(\tau)$ will be:

$$\tilde{\sigma}(\tau) = \frac{1}{K} \sum_{k=1}^{K} \tilde{\sigma}_k(\tau) \tag{3.8}$$

where:

$$\tilde{\sigma}_k(\tau) = \frac{\chi_k(t_k)}{H_k(t_k, \tau)}. \tag{3.9}$$

The procedure described above is applicable to any generic source trajectory. ROSI software was properly developed for rotating paths and it is able to provide optimal results for both constant and slightly variable angular speed, without introducing any further error. Fig. 3.12 clearly shows how the rectangular grid rotates following the single source trajectory.
Since the source signal reconstruction must be carried out for any grid point and for any sampling time, the algorithm computational cost is significant and, as the grid definition increases, it can be several orders of magnitude higher than the VRAM one.

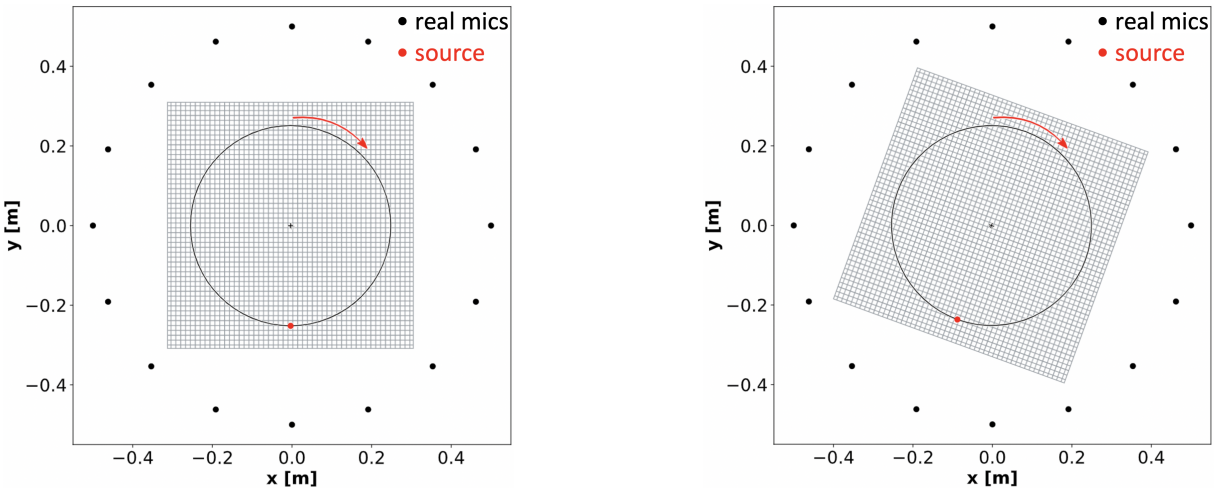

(a) (b)

Figure 3.12: Grid rotation according to ROSI algorithm at: (a) $t = t_0$ (b) $t = t_0 + \Delta t$.

3.5 Time-domain deconvolution methods

As previously stated, the goal of deconvolution methods is to overcome the common issues associated with conventional beamforming, such as too wide beamwidth and the presence of sidelobes. Since frequency-domain beamforming methods for moving sources are limited to only a few special test case geometries, time-domain approaches have emerged within the last decades.
Guérin et al. [23] proposed a hybrid approach in which moving sources were first investigated using time-domain conventional beamforming methods, followed by a deconvolution step employing a PSF that accounts for the Doppler effect. However, this method was able to provide adequate results only when tonal sources were investigated. Another different approach was developed by Fleury and Bulté [24] took a different approach, dividing the sampling time into many snapshots and analyzing each of them with frequency-domain deconvolution algorithms, adding a proper correction for the Doppler frequency shift and amplitude variation. Nevertheless, the most powerful method is Clean-T, which was developed in 2018 by Cousson et al. [10], with the aim of improving the source localization capability and is based on the same concept as the Clean method. The algorithm is fully performed in time-domain and the iterative process presents remarkable differences with the correspondent in frequency-domain. Its logical steps can be summed up throughout the following scheme:

1. The Delay & Sum algorithm is applied to the time data, in order to obtain the "dirty" output signal $\Phi^{(0)}$ at iteration i = 0. At the same time, the "clean" map is initialized:

$$\begin{aligned} \Phi^{(0)}(t,\zeta_j) &= b(t,\zeta_j,p_n) \quad \forall j \in [1;N] \\ \Gamma^{(0)}(t,\zeta_j) &= 0 \\ p_n^{res(0)}(t) &= p_n(t). \end{aligned} \tag{3.10}$$

   For the first iteration, the residual acoustic pressures $p_n^{res(0)}(t)$ are initialized with the ones gathered by the microphone array $p_n(t)$.

2. The dirty map focus point $\hat{\zeta_j}$, which presents the highest energy value, is identified:

$$\hat{\zeta_j} = argmax\left(\int_T |\Phi^{(i-1)}(t,\zeta_j)|^2 dt\right). \tag{3.11}$$

3. Depending on the gain factor value $\gamma \in [0:1]$, the array containing the dirty pressure signals is updated, by removing a fraction of the dominant source contribution:

$$p_n^{res(i)}(t+\frac{r_{\zeta_j n}}{c_0}) = p_n^{res(i-1)}(t+\frac{r_{\zeta_j n}}{c_0}) - \gamma \frac{\Phi^{(i-1)}(t,\hat{\zeta_j})}{r_{\hat{\zeta_j} n}(t)\Big(1 - Mcos\theta_{\hat{\zeta_j} n}(t)\Big)^2} \quad \forall n \in [1;N] \quad (3.12)$$

where c_0 is the acoustic wave propagation speed, $r_{\zeta_j n}$ is the distance between the focus point ζ_j and the microphone n, M is the source Mach number, and $\theta_{\hat{\zeta_j} n}(t)$ is the angle defined by the source trajectory and the direction defined by the segment $r_{\zeta_j n}$.

4. The "clean map" is updated by adding part of the dominant source signal:

$$\Gamma^{(i)}(t,\hat{\zeta_j}) = \Gamma^{(i-1)}(t,\hat{\zeta_j}) + \gamma\Phi^{(i-1)}(t,\hat{\zeta_j}). \quad (3.13)$$

5. Steps 1-4 are iterated until a stopping criterion is reached.

3.6 Acoular

Before focusing the attention on the beamforming algorithms outcomes, it is important to provide a brief introduction of the software employed: Acoular is an open-source object-oriented Python package for processing microphone array data [25]. Nowadays it represents one of the most widespread frameworks in the acoustic community, being capable of implementing several beamforming algorithms, advanced deconvolution methods both in time- and frequency-domain, 3D beamforming and acoustic imaging on both stationary and moving sources. This software significantly improves code performance in terms of time management and computational cost through smart caching and parallel computing (with the optimized Numba compiler), resulting more suitable if compared with other tools.
Before introducing the conclusive chapters, the following paragraphs provide a detailed explanation of the investigated test cases, justifying their utility within this research.

3.7 Analytical benchmarks

Two synthetic test cases, Benchmark A and Benchmark B, were used to evaluate the performances of the various beamforming approaches [26]. Moreover, two different microphone arrays were tested for both benchmarks: one composed of 64 equally spaced sensors located on a ring and the other composed of the same number of sensors but arranged in accordance with Vogel's spiral [27]:

$$r = R\sqrt{\frac{n}{N}} \quad n \in [1; N] \tag{3.14}$$

$$\Phi = 2\pi n \frac{1+\sqrt{V}}{2} \tag{3.15}$$

where V was set equal to 5. This last microphone array geometry was simply named "sunflower", given the analogy with the florets distribution in the sunflower head. Both the arrays were arranged in such a way that their center was aligned with the sources' rotational axis.
The pressure signal time series were always generated with a sampling frequency of 48 kHz and a sampling time of 10 s. The 1 m diameter arrays were placed 0.5 m from the source plane, and a 5 Volt one-trigger-per-revolution signal was generated to simulate the presence of a tachometer.
To generate the beamforming maps a squared grid of 0.6x0.6 m^2 with 3721 nodes was employed.

3.7.1 Benchmark A

The first subcase consists of a single monopolar source following a circular clockwise pattern with a radius of 0.25 m (fig. 3.13). At the trigger instant the source, identified by the number "1", is located at position (0, -0.25 m); moreover, its angular rate is constant and equal to 25 rps and it emits a white noise signal at 94 dB.

3.7.2 Benchmark B

The second test case, on the other hand, features three sound sources rotating clockwise (fig. 3.14), at the same slightly variable rate (fig. 3.15). Their SPL differ from each other: by identifying with the number "1" the dominant one, it is possible to state that $L_{p,1} = L_{p,2}$ + 3 dB = $L_{p,3}$ + 6 dB. Moreover $r_1 = r_2 = 0.25$ m, while $r_3 = 0.125$ m and, at the trigger

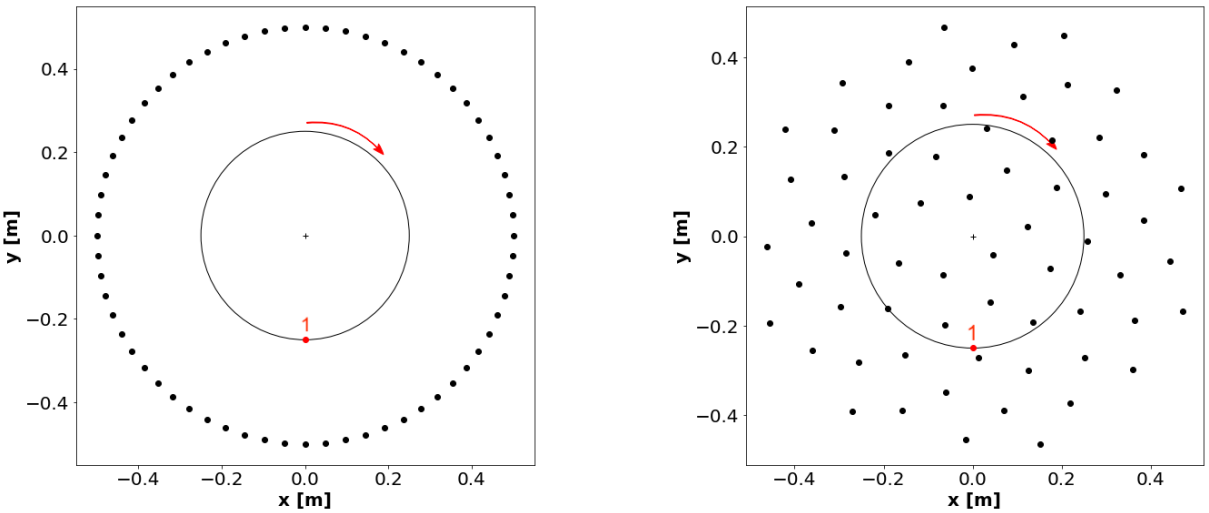

(a) (b)

Figure 3.13: Position of the single source at the trigger instant (red dot) and microphone array setups (black dots): (a) Ring array (b) Sunflower array.

instant, $\beta_1 = \beta_3 = \beta_2$ - 40° = -90°.

Table 3.1 summarizes all of the specifics related to both synthetic test cases.

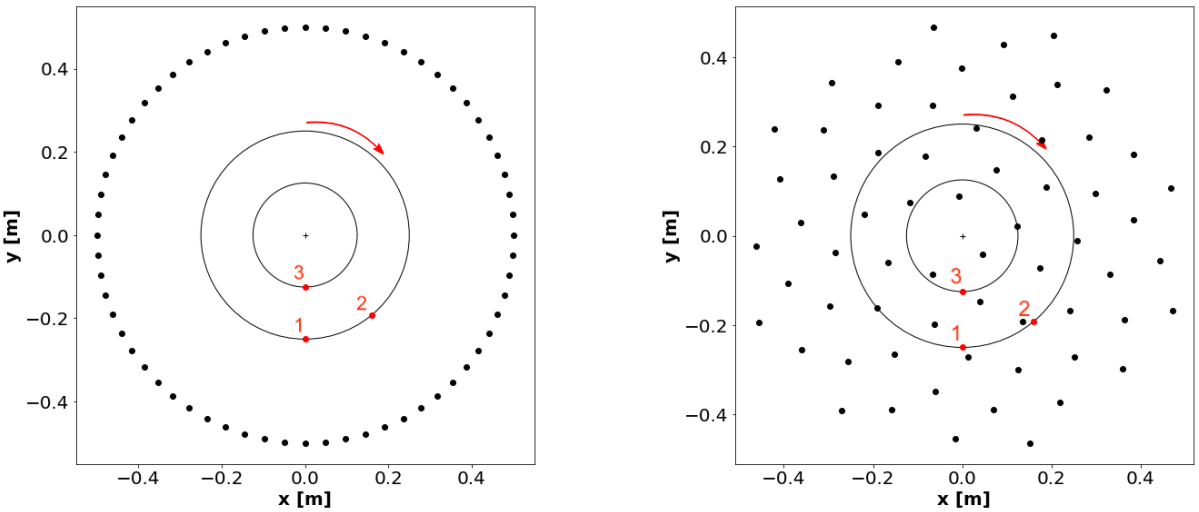

(a) (b)

Figure 3.14: Position of the three sources at the trigger instant (red dot) and microphone array setups (black dots): (a) Ring array (b) Sunflower array.

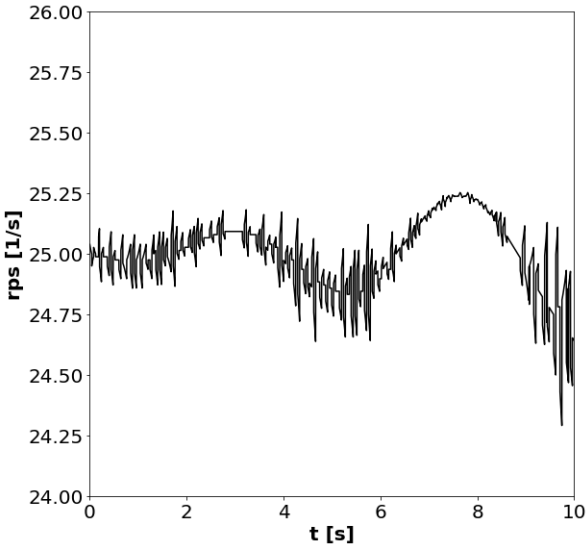

Figure 3.15: Benchmark B: trend of the angular speed during the sampling time.

D_{array}	1 m
$R_1 = R_2 = 2 \cdot R_3$	0.25 m
$L_{p1} = 3\text{dB} + L_{p2} = 6\text{dB} + L_{p3}$	94 dB
z	0.5 m
Sampling frequency	48000 Hz
Measurement time	1 s
FFT block size	1024 samples
FFT window	Hanning, 50 % overlap
Rectangular grid	$x = \pm 0.3$ m $y = \pm 0.3$ m
Grid points	3721
CSM diagonal removal	True
γ	1

Table 3.1: Data-processing parameters of the simulated benchmark data sets.

3.8 Low-pressure axial fan

In addition to the validation steps carried out employing the two benchmarks presented in the previous section, a further analysis was implemented. The sound field of a low-pressure axial fan with un-skewed blades (fig. 3.16) was performed using the data provided by Kaltenbacher et al. [28], in order to test the validated algorithm also with real inputs. Following a detailed description of the experimental setup, the collected data will be processed using conventional beamforming algorithms (ROSI and VRAM) and a time-domain deconvolution method (CleanT). Such final results can be compared to those

presented by the test case author [28], who took advantage of the experiment symmetry to perform the Clean-SC frequency-domain deconvolution method.

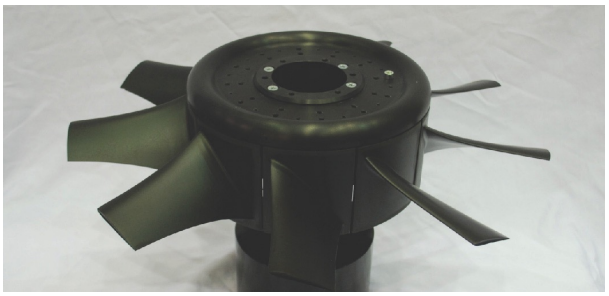

Figure 3.16: Picture of the un-skewed low-pressure axial fan.

3.8.1 Experimental setup

The acquisition step was run in compliance with the standard ISO 5801 [29]; a schematic representation of the benchmark setup is reported in fig. 3.17. The airflow enters the test chamber through a standard bellmouth inlet, and the mass flow rate is controlled by a butterfly damper and an auxiliary fan (to increase it or to decrease it). To keep background noise to a minimum, two flow straighteners are employed: one immediately after the damper and one immediately before the test cell. The low-pressure axial fan is located at the right edge of the test chamber and the airflow is released back into the surrounding environment (fig. 3.18). Its hub is driven by an axial electric motor and its torque is measured through a torque meter mounted on its axis. The rotational speed is computed with the support of an LDA (Laser Doppler Anemometry) system, and the acoustic pressures are measured using 64 microphones arranged on a ring array at a distance of 0.46 m from the fan rotational axis. Furthermore, the sampling frequency was set to 48 kHz for a sampling time of one second.

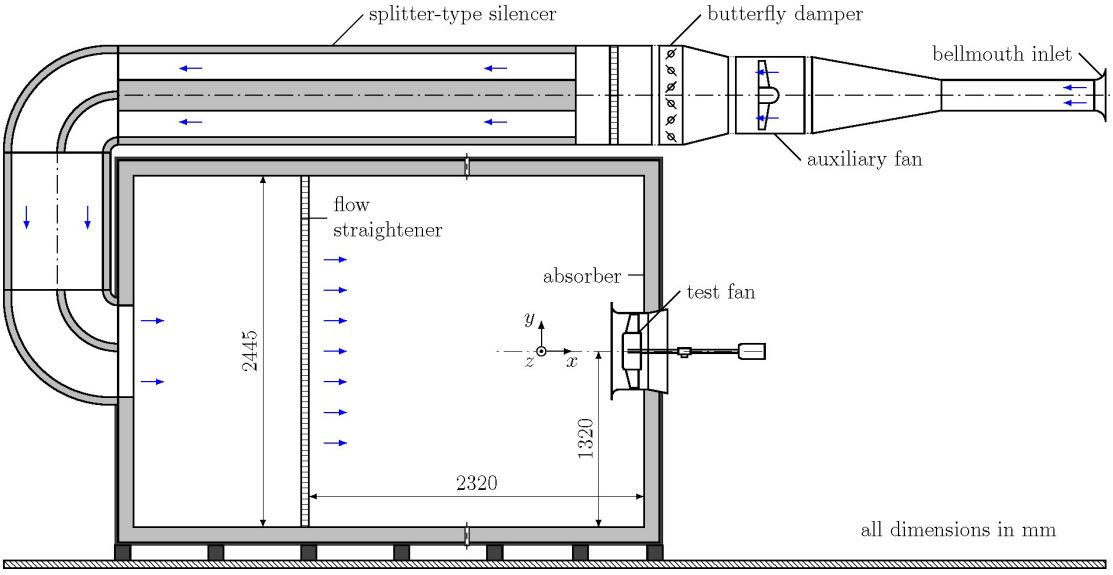

Figure 3.17: Schematic view of the test chamber.

To provide a better understanding of the benchmark geometry, a schematic representation of the test case front view is given in fig. 3.19 a. Instead of using a squared grid, taking advantage of the cylindrical symmetry, it was possible to employ a circular one fig. 3.19 b, with 2656 equally spaced nodes and an external radius of 0.27 m. This resulted in a reduction in algorithm computational cost and an improvement in performance. As for the synthetic benchmark, table 3.2 summarizes all of the specifics related to test case.

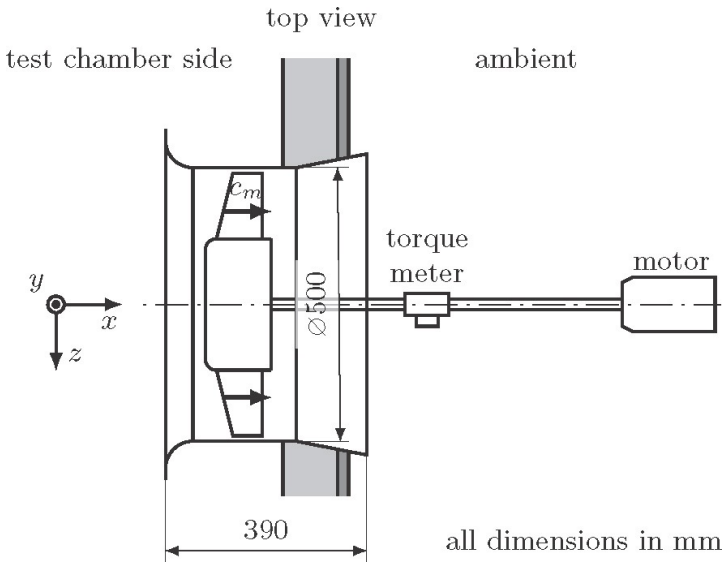

Figure 3.18: Zoom of the fan in the test chamber.

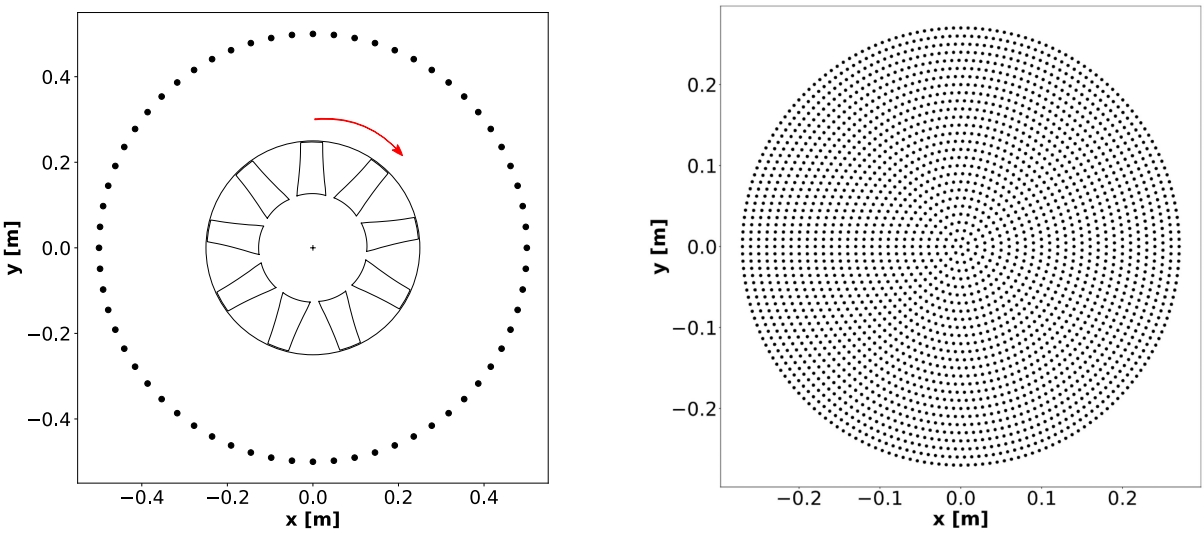

(a) (b)

Figure 3.19: Acoustic investigation of the low-pressure axial fan: (a) Front view of the experimental setup (b) Circular grid.

D_{array}	1 m
z	0.46 m
Sampling frequency	48000 Hz
Measurement time	1 s
FFT block size	1024 samples
FFT window	Hanning, 50 % overlap
Circular grid	$R = 0.27$ m
Grid points	2656
CSM diagonal removal	True
γ	1
Number of iterations	50

Table 3.2: Data-processing parameters of the experimental benchmark data sets.

Chapter 4

Results and Discussion

This chapter contains a discussion of all of the outcomes. To begin, since two microphone array setups were used, the corresponding point spread functions will be shown, highlighting the different performances that can be obtained simply by modifying the array geometry. Following that, all of the beamforming maps for both the synthetic benchmarks and the low-pressure axial fan will be displayed in the same order as in the previous chapter. This will allow us to compare the different algorithms qualitatively and quantitatively, as well as demonstrate how effective microphone array methods can be in understanding sound generation mechanisms.

4.1 Point Spread Functions

As underlined several times, the PSF depends on the array dimension, the number and distribution of microphones and the inspected frequency band. Throughout its analysis, it is possible to quantify the acquiring system's performance by estimating a few parameters such as beamwidth and sidelobe ratio.
The results displayed in the following sections have been obtained employing two devices with the same size and number of sensors: a ring array with equally spaced microphones and a sunflower array (fig. 3.13 a and 3.13 b). Fig. 4.1 and fig. 4.2 show the PSF of both the arrays at the third-octave frequency bands of $f_c = 2500$ Hz, $f_c = 5000$ Hz and $f_c = 10000$ Hz and with a dynamic range of 20 dB, while table 4.1 compares the performance parameters.
As it is possible to state, the ring array offers better performances in terms of spatial resolution, indeed, the circular disposition of the whole set of microphones guarantees lower

beamwidths at each frequency band. On the other hand, the uneven and non-redundant arrangement in the sunflower geometry ensures higher sidelobe ratios, reducing the issues associated with spurious sources. Most of the time, a better sidelobe suppression is preferred over the detection of thinner main lobes, which is enough to justify the use of spiral arrays. However, as will be demonstrated later, especially in the case of rotating sources, the algorithm selection may represent a more binding constraint.
Since different microphone numbers are taken into account in the case of the sunflower array, it is critical to understand how the PSF changes: as the number of sensors increases, the main lobe width remains relatively constant while the sidelobe ratio rapidly grows.

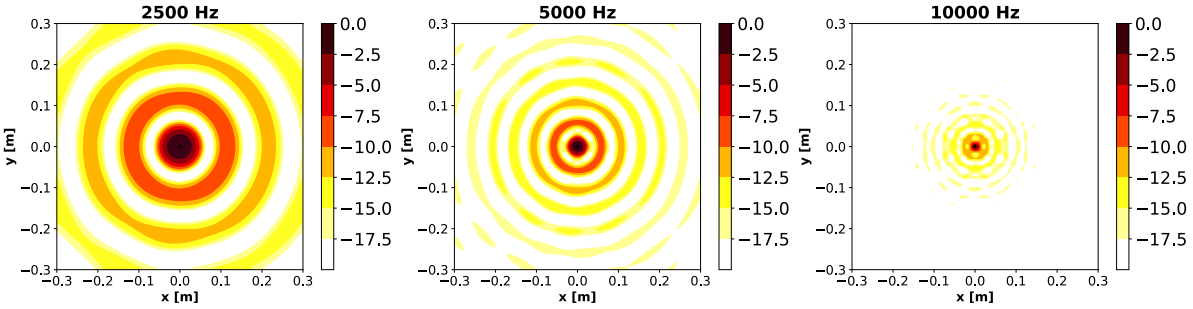

(a) (b) (c)

Figure 4.1: Ring array PSF at (a) 2500Hz. (b) 5000Hz. (c) 10000Hz.

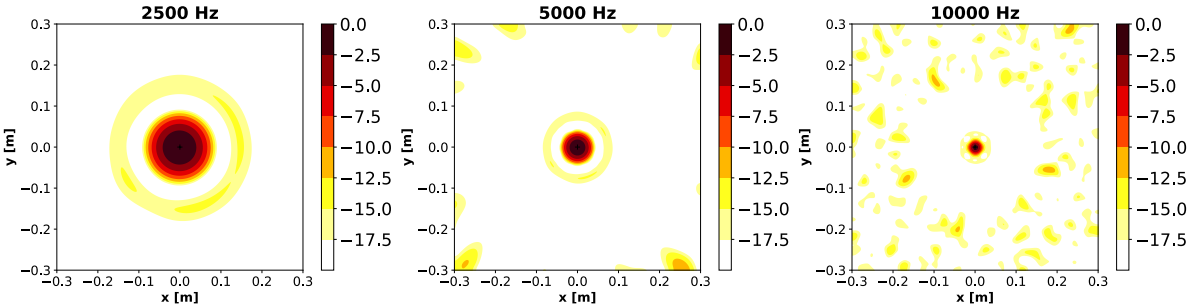

(a) (b) (c)

Figure 4.2: Sunflower array PSF at (a) 2500Hz. (b) 5000Hz. (c) 10000Hz.

		Beamwidth [m]	**SLR [dB]**
Ring array	2500 Hz	0.07	8.60
	5000 Hz	0.04	8.40
	10000 Hz	0.02	8.30
Sunflower array	2500 Hz	0.10	15.00
	5000 Hz	0.05	14.75
	10000 Hz	0.02	14.60

Table 4.1: Comparison between the performances of the ring array and the sunflower one

4.2 Virtual Rotating Array Method (VRAM)

Fig. 4.3 and fig. 4.4 respectively display the beamforming maps related to the benchmark A and B for the third-octave frequency bands: $f_c = 2500$ Hz, $f_c = 5000$ Hz, $f_c = 10000$ Hz.

As it was demonstrated by Ocker et al. [30], the employment of a ring array can ensure optimal results with frequency-domain methods and both constant and slightly variable rotating speed.

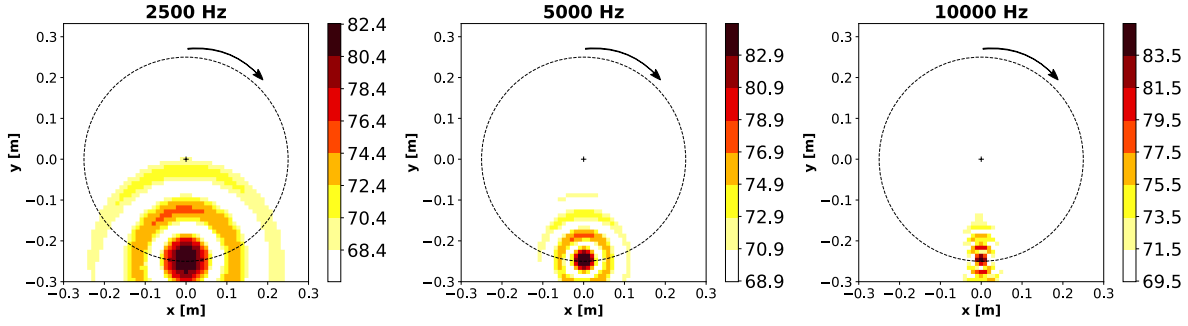

(a) (b) (c)

Figure 4.3: Benchmark A: VRAM beamforming map at (a) 2500Hz. (b) 5000Hz. (c) 10000Hz.

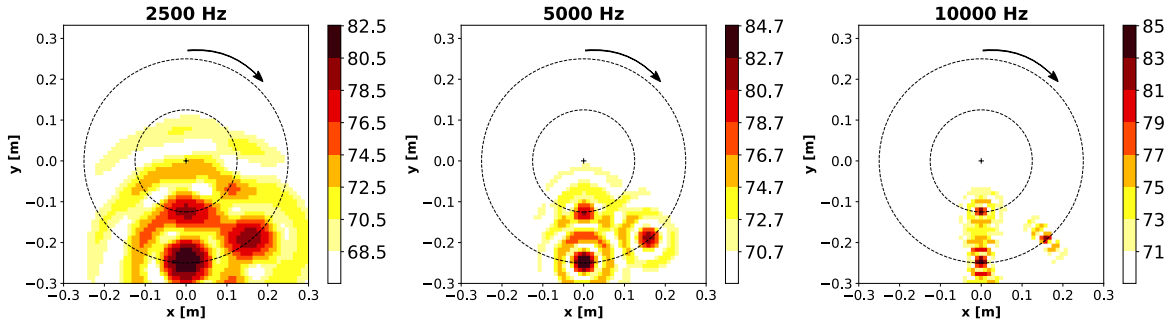

(a) (b) (c)

Figure 4.4: Benchmark B: VRAM beamforming map at (a) 2500Hz. (b) 5000Hz. (c) 10000Hz.

4.3 VRAM with irregularly shaped microphone array

To validate the VRAM with irregularly shaped microphone arrays, the synthetic benchmarks were investigated by using a sunflower array (fig. 3.13 b and 3.14 b).
Fig. 4.6 shows the third-octave band beamforming maps evaluated at $f_c = 2500$ Hz, $f_c = 5000$ Hz and $f_c = 10000$ Hz by applying the algorithm written by Jekosch, while fig. 4.8 displays results provided after introducing the correction proposed in this study.

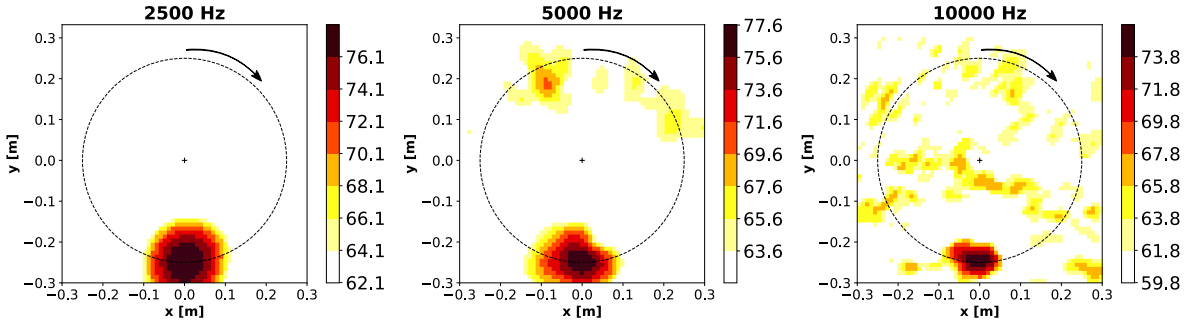

Figure 4.5: Benchmark A: Jekosch's VRAM extension beamforming map at (a) 2500Hz. (b) 5000Hz. (c) 10000Hz, with 64 sensors.

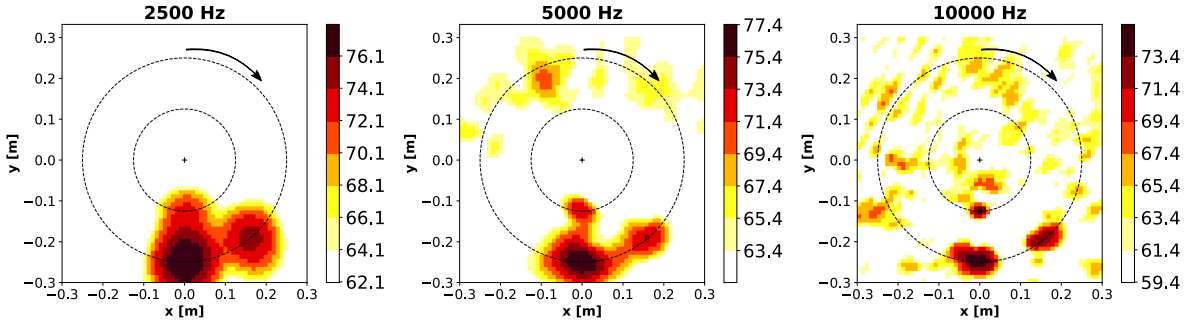

Figure 4.6: Benchmark B: Jekosch's VRAM extension beamforming map at (a) 2500Hz. (b) 5000Hz. (c) 10000Hz, with 64 sensors.

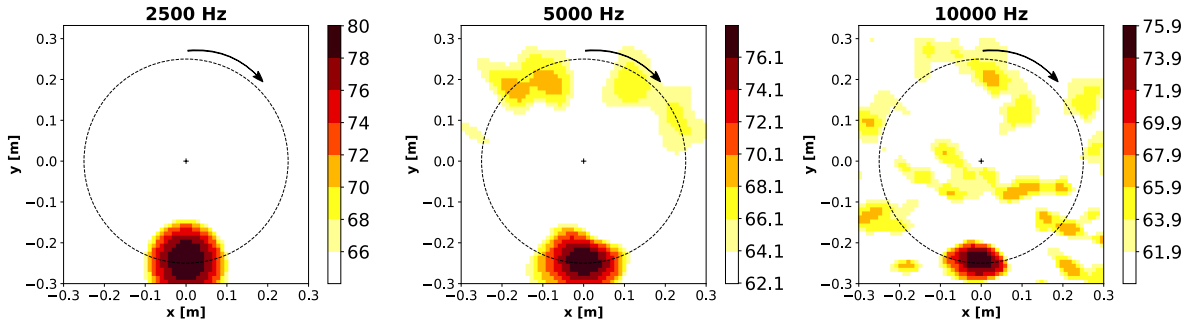

(a) (b) (c)

Figure 4.7: Benchmark A: Modified VRAM extension beamforming map at (a) 2500Hz. (b) 5000Hz. (c) 10000Hz, with 64 sensors.

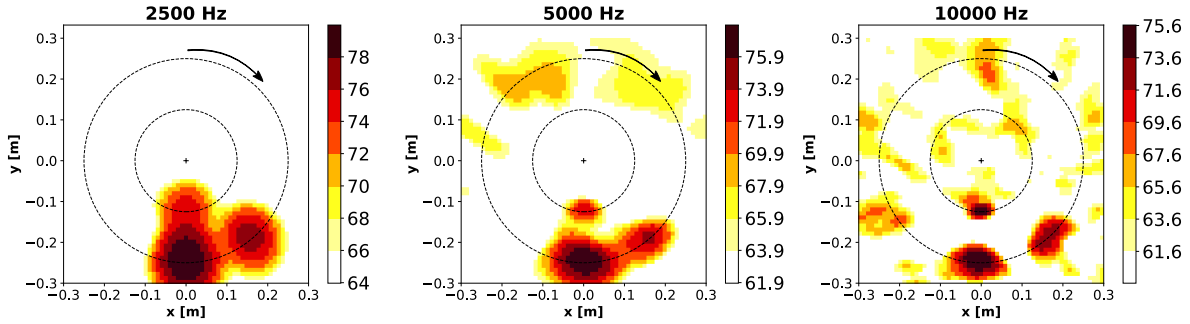

(a) (b) (c)

Figure 4.8: Benchmark B: Modified VRAM extension beamforming map at (a) 2500Hz. (b) 5000Hz. (c) 10000Hz, with 64 sensors.

Even if the computational cost is comparable, it is possible to notice that the sources are better identified in the latter case: the maximum SPL is closer to the target, the beamwidth is lower, and the sidelobe ratio is higher.
Nonetheless, the results of this last method are far from satisfactory. To better understand its inner physical limits, a second analysis was performed using the same sunflower geometry but with a different number of sensors. Fig. 4.10 and fig. 4.12 respectively display the outcomes provided by using 32 and 128 microphones.

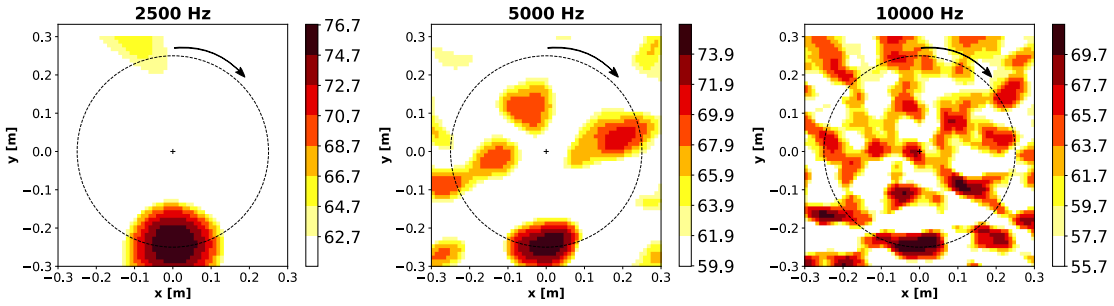

(a) (b) (c)

Figure 4.9: Benchmark A: Modified VRAM extension beamforming map at (a) 2500Hz. (b) 5000Hz. (c) 10000Hz, with 32 sensors.

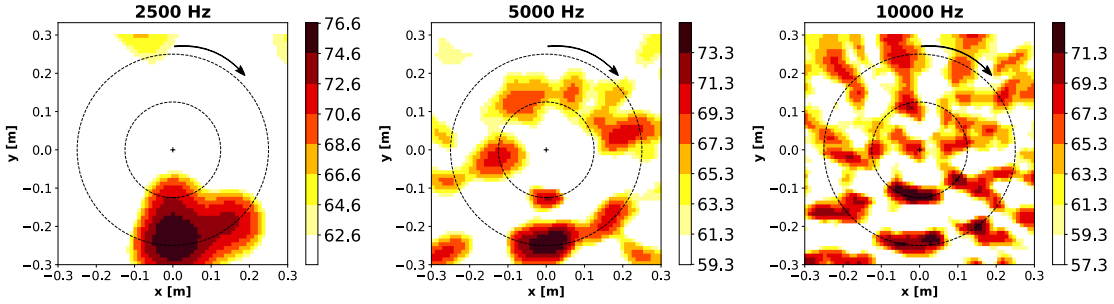

(a) (b) (c)

Figure 4.10: Benchmark B: Modified VRAM extension beamforming map at (a) 2500Hz. (b) 5000Hz. (c) 10000Hz, with 32 sensors.

By increasing the number of microphones, and thus the equipment cost, it is possible to achieve more detailed beamforming maps, especially at higher frequencies, but anyway, the performances do not come close to those obtained with the conventional VRAM.
To provide a quantitative result, a further study was carried out employing just the benchmark A: after defining a squared integration sector of 0.02x0.02 m^2 around the SPL peak value, a comparison was developed between the ring array with 64 sensors and the sunflower ones with a different number of microphones (fig. 4.13). By constructing the integrated spectra, it was possible to determine how far their performances extend and at what frequency irregularly shaped arrays can provide reliable information.
The acoustic wavelength is a few orders of magnitude larger than the distance between two adjacent microphones at low frequencies, ensuring high reliability to the mesh-based interpolation process; however, as the inspected frequency increases, the real acoustic field pattern dramatically differs from the interpolated one, causing a drop in performance.

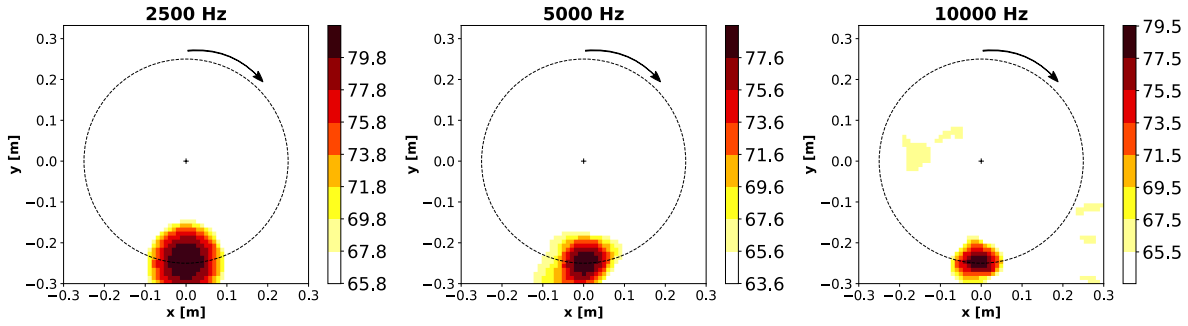

Figure 4.11: Benchmark A: Modified VRAM extension beamforming map at (a) 2500Hz. (b) 5000Hz. (c) 10000Hz, with 128 sensors.

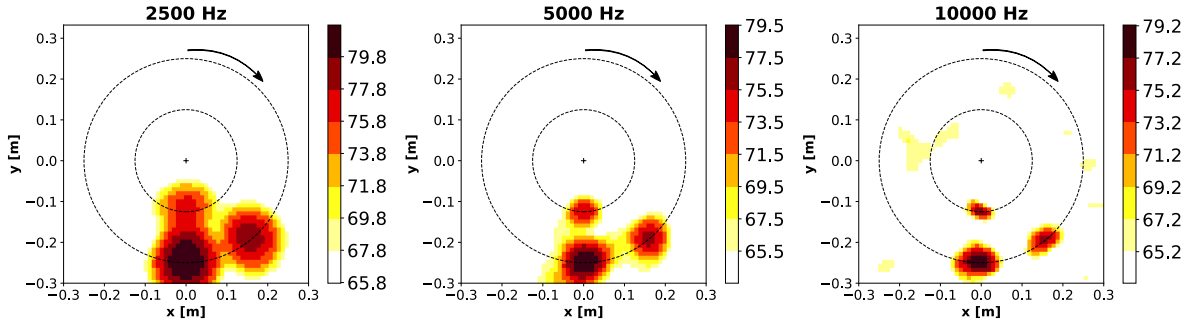

Figure 4.12: Benchmark B: Modified VRAM extension beamforming map at (a) 2500Hz. (b) 5000Hz. (c) 10000Hz, with 128 sensors.

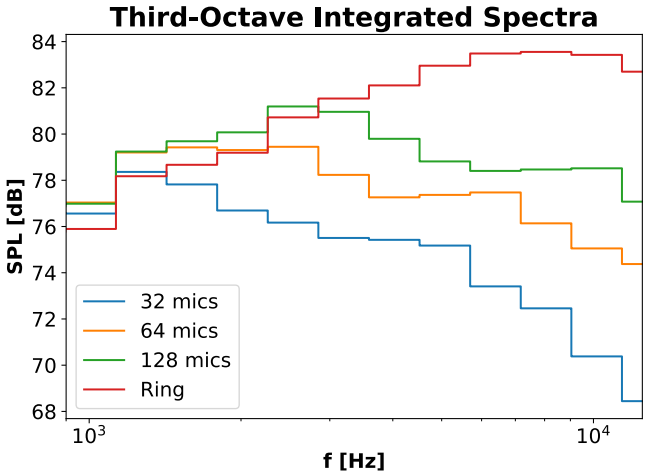

Figure 4.13: Benchmark A: third-octave integrated spectra.

4.4 ROSI

After validating all the discussed frequency-domain methods, the focus is shifted to time-domain approaches. Fig. 4.14 and fig. 4.15 respectively illustrate the sound maps for the benchmarks A and B, for the third-octave bands: $f_c = 2500$ Hz, $f_c = 5000$ Hz, $f_c = 10000$ Hz. All of the acoustic sources are perfectly identified and the SPL are similar to the ones outlined by executing the VRAM method, with an error on the peak value lower than 2 dB. However, a significant difference lies in the computational effort: as stressed out previously, ROSI requires ~ 10 times the cost needed by VRAM.

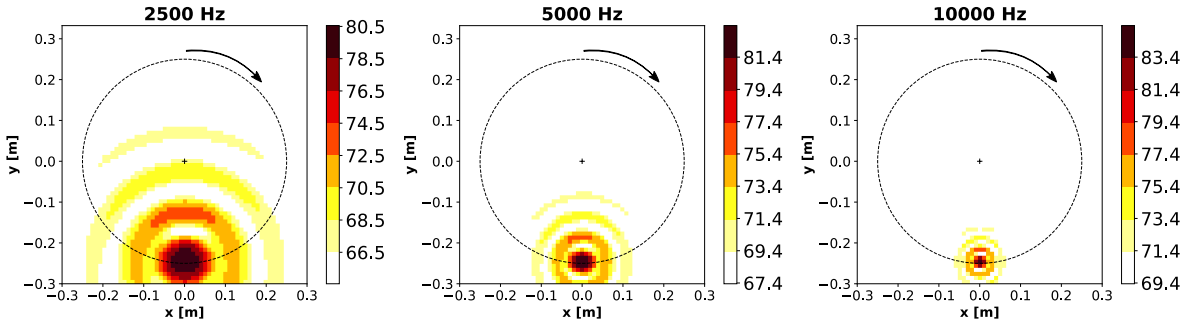

(a) (b) (c)

Figure 4.14: Benchmark A: ROSI beamforming map at (a) 2500Hz. (b) 5000Hz. (c) 10000Hz.

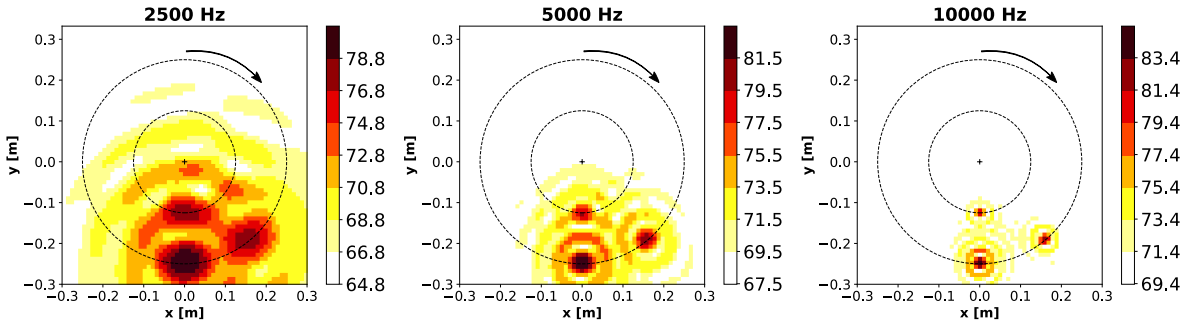

(a) (b) (c)

Figure 4.15: Benchmark B: ROSI beamforming map at (a) 2500Hz. (b) 5000Hz. (c) 10000Hz.

		$\mathbf{SPL_{max}}$ [dB]	Beamwidth [m]	SLR [dB]
VRAM	2500 Hz	82.40	0.08	7.50
	5000 Hz	84.85	0.04	8.30
	10000 Hz	85.46	0.02	4.90
Jekosch VRAM extension	2500 Hz	78.08	0.11	19.50
	5000 Hz	77.62	0.10	9.00
	10000 Hz	75.78	0.09	8.90
Modified VRAM extension 32 mics	2500 Hz	76.75	0.14	6.60
	5000 Hz	75.87	0.11	4.80
	10000 Hz	71.76	0.11	1.00
Modified VRAM extension 64 mics	2500 Hz	80.02	0.14	19.50
	5000 Hz	78.06	0.10	9.00
	10000 Hz	75.92	0.09	6.20
Modified VRAM extension 128 mics	2500 Hz	81.79	0.12	16.80
	5000 Hz	79.56	0.08	17.10
	10000 Hz	79.53	0.07	15.20
ROSI	2500 Hz	80.55	0.08	7.00
	5000 Hz	83.35	0.04	7.20
	10000 Hz	85.35	0.02	7.30

Table 4.2: Benchmark A: comparison between the performances of the different algorithms.

4.5 Clean-T

The CleanT deconvolution method was the final method validated using synthetic benchmarks. Fig. 4.16 and fig. 4.17 show the results for the two test cases, demonstrating how effective this deconvolution method is: in both examples, all sources are perfectly separated and identified at every frequency band.

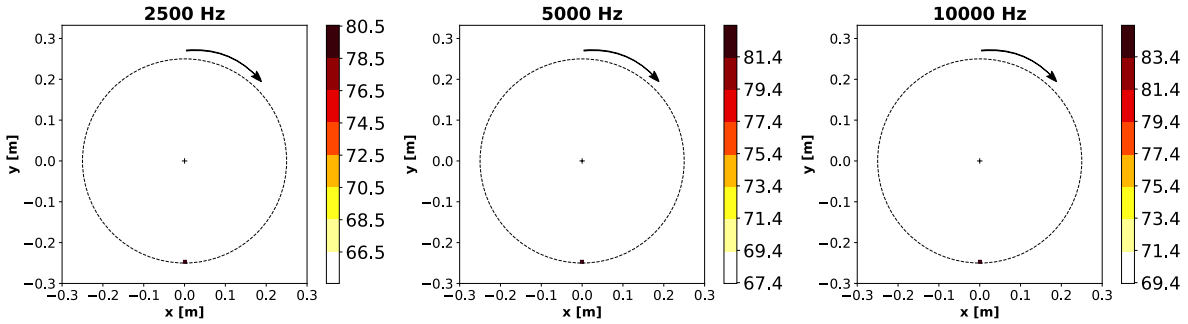

(a) (b) (c)

Figure 4.16: Benchmark A: CleanT beamforming map at (a) 2500Hz. (b) 5000Hz. (c) 10000Hz.

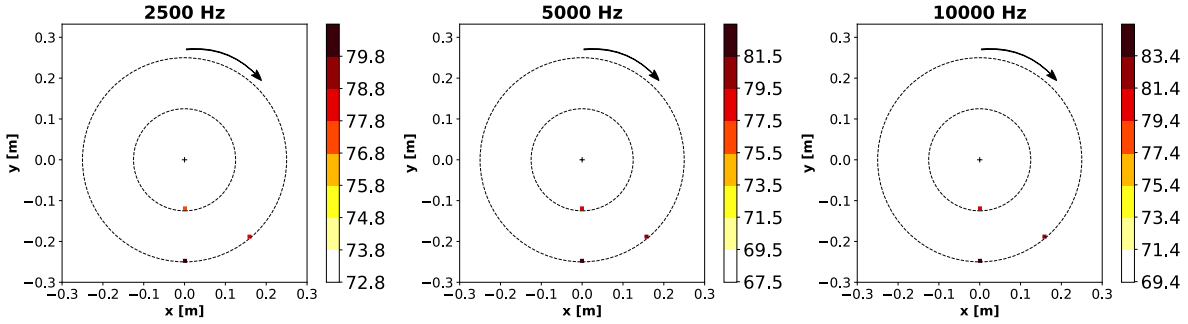

(a) (b) (c)

Figure 4.17: Benchmark B: CleanT beamforming map at (a) 2500Hz. (b) 5000Hz. (c) 10000Hz.

4.5.1 Low-pressure axial fan

Once the validation step has drawn to an end, it is possible to show how these beamforming algorithms perform in the case of real experimental data, studying the noise emission of a low-pressure axial fan.
The first acoustical analysis was carried out by applying both time- and frequency-domain algorithms for rotating frameworks: fig. 4.19 displays the maps generated by ROSI and fig. 4.18 shows the output provided by VRAM. Both methods were tested at three different third-octave frequencies: 2 kHz, 4 kHz, and 5 kHz.

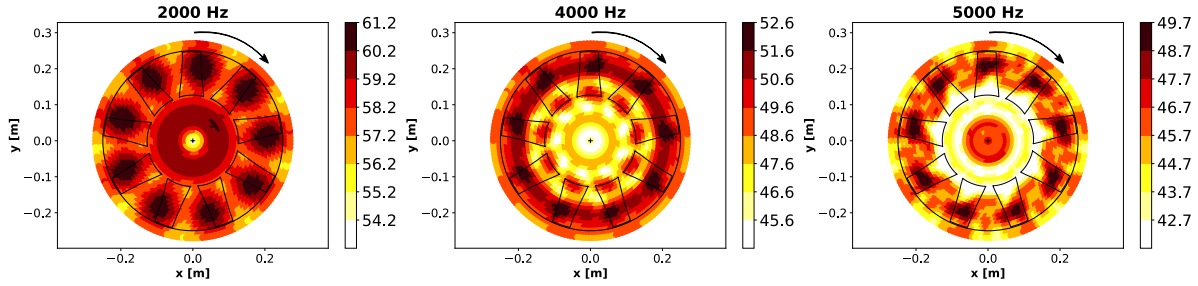

(a) (b) (c)

Figure 4.18: VRAM beamforming map at (a) 2000Hz. (b) 4000Hz. (c) 5000Hz.

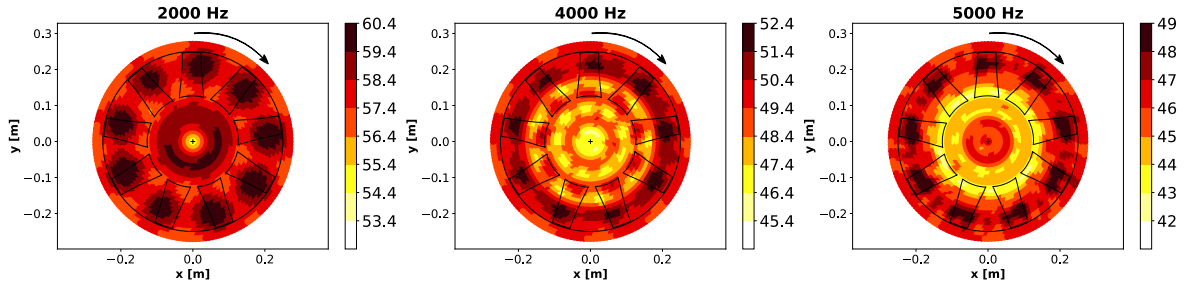

(a) (b) (c)

Figure 4.19: ROSI beamforming map at (a) 2000Hz. (b) 4000Hz. (c) 5000Hz.

As mentioned in Chapter 3, traditional beamforming methods produce quite blurry results with a low sidelobe ratio. To avoid this problem, the option of using an iterative deconvolution method such as CleanT was introduced. Fig. 4.20 shows the results of 50 CleanT iterations for the same third-octave bands.

Unsurprisingly, all of the significant noise sources are located near the tips of the blades. This is primarily due to the faster blade circumferential speed, but it is also due to the presence of duct walls and tip leakage flow. By focusing on the different central frequencies,

two main sound generation mechanisms can be seen, which justify the sources' azimuthal positions. Up to $f_c = 4000$ Hz leading-edge noise is the dominant mechanism: as explained by Zarri et al. [31], turbulent flow velocity fluctuations produce a local random variation of the blades incidence angle, and thus random pressure fluctuations are created on the leading-edge, resulting in broadband noise. At $f_c = 5000$ Hz trailing-edge noise, also known as self-noise, predominates. This acoustic mechanism, which generates broadband noise, is caused by the interaction of swirling structures (which characterize a turbulent boundary layer) and the trailing edge of the blade.

This final consideration concludes the results section. Chapter 5 will collect all the conclusions related to this work, drawing further perspectives for future research.

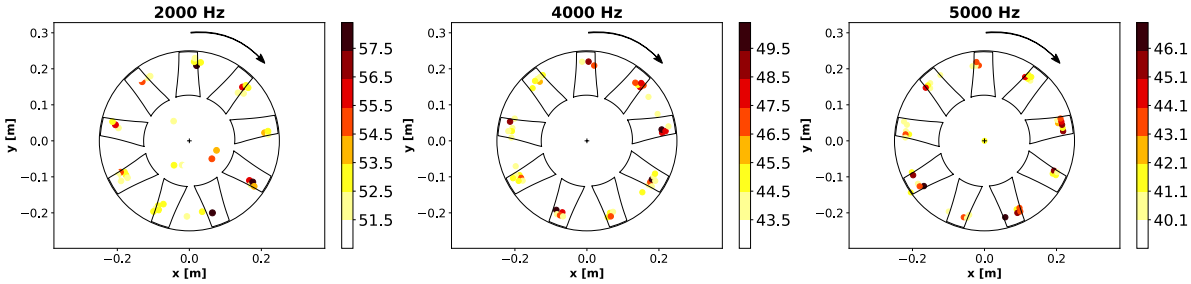

(a) (b) (c)

Figure 4.20: CleanT beamforming map at (a) 2000Hz. (b) 4000Hz. (c) 5000Hz.

Chapter 5

Conclusion and future perspectives

The work presented here was completed as part of a Short Training program at the von Karman Institute for Fluid Dynamics' Environmental & Applied Fluid Dynamics department in Belgium. Its goal has been to provide a more comprehensive understanding of conventional and advanced acoustic beamforming techniques for investigating noise sources in rotating frameworks. Since interest in such techniques has steadily grown in recent decades, and powerful methods have been developed, this study has been carried out in an attempt to understand the inherent limits and, eventually, to improve the current state of the art.

The first step in the research was to become acquainted with the theory of acoustic wave propagation in order to properly handle the physics of this mechanism. As a result, conventional beamforming methods for stationary sources, both in the time- and frequency-domain, have been studied in-depth in order to understand their strengths and weaknesses, and their extensions for rotating sources have been introduced once their implementations were clear. The emphasis was primarily on both the ROSI and VRAM algorithms, which were thoroughly explained in the third chapter. After developing them, it was possible to summarize their performances: ROSI, which is based on a time-domain approach, can deal with any microphone array geometry and spatial location relative to the rotating machine, allowing the use of optimized phased arrays, but taking a long time. VRAM, on the other hand, can reduce computational costs by more than ten times and allows

for the use of advanced beamforming techniques such as the GIBF, but it is limited by a few geometrical constraints; for example, the microphone array must be circular and its centre must be perfectly aligned with the inspected object's rotational axis. To take advantage of the strengths of frequency-domain beamformers, an extension of the VRAM algorithm for irregularly shaped microphone arrays was studied and optimized until its intrinsic limit was reached. Finally, deconvolution methods in the frequency (Clean and Clean-SC) and time (CleanT) domains have been introduced to improve the ability to discern noise sources in an acoustic map more intuitively. To validate all of the methods mentioned above, two synthetic benchmarks with different characteristics have been used: the first (benchmark A) featured a single point source rotating at a constant angular rate, while the second (benchmark B) featured three different point sources rotating at the same variable angular rate. The validation process was followed by an acoustic investigation of an experimental test case: relying on the data published by Kaltenbacher et al. [28], the sound emission of an un-skewed low-pressure axial fan was completed in order to understand the algorithms' performance on real setups. All numerical analyses were carried out in Acoular, an open-source software written in Python and widely used in the aeroacoustic community.

Several conclusions could be drawn from the results of such analysis. The mesh-based approach that underpins the VRAM extension for irregularly shaped microphone arrays has yielded unsatisfactory results. The linear interpolation produces too blurred acoustic maps, which can only be accepted for very low-frequency bands, and increasing the number of sensors does not improve the map definition significantly. Furthermore, there is always the need to perfectly align the rotating machine axis with the phased array centre, and many wind tunnels lack the space to meet this requirement. However, if this last constraint can be overcome, it is always recommended to invest resources in a ring-shaped microphone array. In this case, depending on the array dimension and the number of microphones, the interpolation process is reliable up to very high-frequency bands, the computational cost is minimized, and all the advanced methods that require the cross-spectral matrix calculation can be used. If, on the other hand, it is not possible to align the array centre with the rotating framework axis, it is recommended to direct all the effort toward time-domain methods such as ROSI and toward an optimized array geometry, resulting in a very detailed beamforming map but with high time investment.
Nevertheless, to improve the source visualization even further, the CleanT deconvolution method can be used, which, despite its inherent limitations, can produce excellent results.

Indeed, by deconvoluting the acoustic signals in the beamforming map, it is possible to precisely locate dominant sound sources and inspect also previously unknown secondary noise generation mechanisms. Despite this, CleanT does not support any automatic procedure for determining the stopping criteria and does not permit an efficient investigation of distributed sources.

In the coming years, following the current trend of microprocessors evolution, computing power will significantly increase, reducing the major drawback of time-domain beamforming methods. Nevertheless, further enhancements to the CleanT deconvolution method are expected in order to fully benefit from its potential: currently, in addition to the inability to inspect distributed sources, the number of iterations must be known in advance and these issues limit the algorithm performance. On the other hand, also frequency-domain beamforming techniques for rotating sources can be improved. Their main problems are the coaxiality bound between the microphone array center and the source's rotational axis, as well as the dependence on an interpolation process. The breaking down of these barriers will allow for significant advancements in acoustic beamforming methods, having a huge impact on the aeroacoustic community.

Bibliography

[1] B. Valentine. «Noise pollution in Port Harcourt metropolis: sources, effect, and control». In: *The Pacific Journal of Science and Technology* (2010) (cit. on p. 1).

[2] R. Zamponi. *Development of acoustic beamforming techniques for acoustic wiind-tunnel tests.* Rhode Saint Genèse, 2015 (cit. on pp. 2, 8).

[3] U. Micheal. «History of acoustic beamforming». In: *BeBeC* (2006) (cit. on p. 2).

[4] R. Kinns J. Billingsley. «The acoustic thelescope». In: *Journal of Sound and Vibrations* (1976) (cit. on p. 2).

[5] E. Sarradj. «A generic approach to synthsizeoptimal array microphone arrangements». In: *BeBeC* (2016) (cit. on pp. 2, 14).

[6] R. Dougherty. «Spiral-shaped array for broadband imaging Pat». In: *US 5,838,284* (1998) (cit. on p. 2).

[7] T. Susuki. «Generalized Inverse Beam-forming Algorithm Resolving Coherent/Incoherent, Distributed and Multipole Sources». In: *14th AIAA/CEAS Aeroacoustics Conference (29th AIAA Aeroacoustics Conference)* (2008) (cit. on p. 2).

[8] E. Sarradj G. Herold. «Microphone array method for the characterization of rotating sound sources in axial fans». In: *NCEJ* (2015) (cit. on pp. 3, 19).

[9] E. Sarradj S. Jekosch. «An Extension of the Virtual Rotating Array Method Using Arbitrary Microphone Configurations for the Localization of Rotating Sound Sources». In: *Acoustics Journal* (2020) (cit. on pp. 3, 24, 25).

[10] R. Cousson. «A time domain CLEAN approach for the identification of acoustic moving sources». In: *Journal of Sound and Vibration* (2018) (cit. on pp. 9, 12, 33).

[11] P. Sijtsma R. Merino-Martinez. «A review of acoustic imaging methods using phased microphone arrays». In: *CEAS Aeronautical Journal* (2019) (cit. on p. 12).

[12] E. Sarradj. «Three-Dimensional Acoustic Source Mapping with Different Beamforming Steering Vector Formulations». In: (2012) (cit. on p. 12).

[13] W. Devenport S. Glegg. *Aeroacoustic of low mach number flows*. Elsevier (cit. on p. 13).

[14] Leandro de Santana. «Fundamentals of Acoustic Beamforming». In: *NATO* () (cit. on p. 14).

[15] M. A. F. de Medeiros F. R. do Amaral J. C. S. Rico. «The Thermodynamics of Wake Blade Interaction in Axial Flow Turbines: Combined Experimental and Computational Study». In: *Journal of the Brazilian Society of Mechanical Sciences and Engineering* (2018) (cit. on p. 14).

[16] M.-A. Pallas. «Localisation des sources de bruit des transports guidés (localization of noise sources on guided vehicles), Instrumentation Mesure Métrologie». In: (2002) (cit. on p. 15).

[17] R. Stoker P. Sijtsma. «Determination of Absolute Contributions of Aircraft Noise Components Using Fly-over Array Measurements». In: *American Institute of Aeronautics and Astronautics* (2004) (cit. on p. 15).

[18] S. Oerlemans. *Detection of aeroacoustic sound sources on aircraft and wind turbines*. National Aerospace Laboratory NLR, 2009 (cit. on p. 15).

[19] P. Chiariotti. *Acoustic beamforming for noise source localization – Reviews, methodology and applications*. Vol. Mechanical Systems and Signal Processing. 2018 (cit. on p. 29).

[20] R. P. Dougherty. «Sidelobe suppression for phased array aeroacustic measurements». In: *Conference of European Aerospace Societies* (1998) (cit. on p. 29).

[21] P. Sijtsma. «CLEAN based on spatial source coherence». In: *international journal of aeroacoustics* (2007) (cit. on p. 29).

[22] S. Oerlemans P. Sijtsma. «Location of rotating sources by phased array measurements». In: *CEAS Aeroacoustics conference* (2001) (cit. on p. 31).

[23] C.Weckmüller S. Guérin. «Frequency-domain reconstruction of the point spread function for moving sources». In: *BeBeC* (2008) (cit. on p. 33).

[24] J. Bulté V. Fluerty. «Extension of deconvolution algorithms for the mapping of moving acoustic sources». In: *Journal of the Acoustical Society of America* 129 (2011) (cit. on p. 33).

[25] G. Herold E. Sarradj. «A Python framework for microphone array data processing». In: *Applied Acoustics* 116 (2017) (cit. on p. 34).

[26] G. Herold. «Microphone Array Benchmark b11: Rotating Point Sources». In: (2019) (cit. on p. 35).

[27] H. Vogel. «A better way to build the sunflower head». In: *Mathematical biosciences* (1979) (cit. on p. 35).

[28] M. Kaltenbacher F. Zenger C. Junger and S. Becker. «A Benchmark Case for Aerodynamics and Aeroacoustics of a Low Pressure Axial Fan». In: *SAE international* (2016) (cit. on pp. 37, 38, 58).

[29] «ISO 5801 - Fans - Performance testing using standardized airways». In: (2017) (cit. on p. 39).

[30] C. Ocker. «A comparison of frequency-domain microphone array methods for the characterization of rotating broadband noise sources». In: *Acta Acustica united with America* (2018) (cit. on p. 46).

[31] C. Schram A. Zarri J. Christophe. «Low-Order Aeroacoustic Prediction of Low-Speed Axial Fan Noise». In: *25th AIAA/CEAS Aeroacoustics Conference* (2019) (cit. on p. 55).